A kinetic model of oriented nucleation under nonhydrostatic stress: Implications for the preferred orientation of columnar and platy minerals in metamorphic rocks

1 A kinetic model of oriented nucleation under nonhydrostatic stress: implications for

2 the preferred orientation of columnar and platy minerals in metamorphic rocks

3

4 Toshiaki MASUDA[1,2*]

5 [1]Institute of Geosciences, Shizuoka University, Ohya 836, Suruga-ku, Shizuoka 422–8529, Japan

6 [2]Present address: Center for Integrated Research and Education of Natural Hazards, Shizuoka

7 University, Ohya 836, Suruga-ku, Shizuoka 422-8529, Japan

8 and

9 Yasutomo OMORI[2,3]

10 [2]Center for Integrated Research and Education of Natural Hazards, Shizuoka University, Ohya 836,

11 Suruga-ku, Shizuoka 422-8529, Japan

12 [3]Present address: Department of Mathematical Science and Advanced Technology, JAMSTEC,

13 Natsushima 2-15, Yokosuka, 237-0061, Japan

14

15 *Corresponding author

16 Toshiaki MASUDA

17 E-mail: masuda.toshiaki@shizuoka.ac.jp

18 Tel: +81–542384785

19 Postal address: Center for Integrated Research and Education of Natural Hazards, Shizuoka

20 University, Ohya 836, Suruga-ku, Shizuoka 422-8529, Japan

21

24   Abstract

25   We propose a kinetic model for the nucleation rate of columnar and platy

26   minerals in nonhydrostatically stressed metamorphic rocks. Nucleation rate I in our

27   model is expressed as

28

29     $$I(T, \sigma_n) = A exp\left(-\frac{\Delta U^* - T\Delta S^* + \sigma_n \Delta V^*}{k_B T}\right),$$

30

31   Where ΔU^*, ΔS^* and ΔV^* are the internal energy, entropy and volume of activation,

32   respectively, k_B is the Boltzmann constant, T is absolute temperature, σ_n is the

33   magnitude of the normal stress applied to the site of heterogeneous nucleation, and

34   A is a constant. As σ_n varies with respect to the spatial orientation of the nucleation

35   site in nonhydrostatically stressed rocks, the nucleation rate I also varies

36   accordingly. As the number of nucleated grains is proportional to I, anisotropic

37   nucleation can produce a preferred orientation of mineral grains. The model predicts

38   the von Mises distributions of the long axes of columnar mineral grains and poles to

39   the basal planes of platy mineral grains on any plane cut perpendicular to the

40   principal-stress axes. The model also uses the exponential form of the Lamé's stress

41   ellipsoid to plot contoured equal-area stereographic fabric diagrams. As the

42   generated patterns are similar to those observed in metamorphic rocks, the model is

43   likely useful for analyses of natural deformation.

1. Introduction

Crystal nucleation is a key process during the evolution of the Earth because 'the solid Earth consists of very approximately 10^{30} crystals, most of which were created by processes of nucleation and growth' (Kretz, 1994, p. 300). In this study we consider the nucleation of several metamorphic minerals and the origin of preferred orientations formed under a nonhydrostatic stress state.

Thermodynamics allows the prediction of which minerals will be stable under given temperature and pressure conditions (e.g., Spear, 1993; Vernon and Clarke, 2008). Previous studies have attempted to formulate nonhydrostatic thermodynamic equations and use them to predict the preferred orientation of minerals under nonhydrostatic stress states (e.g., Kamb, 1959; Kumazawa, 1963; Paterson, 1973). However, these studies are unsatisfactory to predict the wide range of preferred orientation patterns of natural mineral grains. Although the occurrence of metamorphic minerals is controlled mainly by thermodynamics, several other factors have been recognised. For example, diamond exists in a stable state at ambient temperatures and pressures, despite being thermodynamically unstable. This is due to a sluggish transformation rate from diamond to graphite due to a high activation energy (e.g., Putnis and McConnell, 1980). This example shows that kinetics, in addition to thermodynamics, plays a significant role during metamorphic mineral transformations (Fig. 1a).

'insert Fig. 1'

We focus on the kinetics of nucleation and propose a model for anisotropic nucleation rates in nonhydrostatically stressed rocks. The kinetic model may be a powerful tool to predict the preferred orientation of platy minerals (e.g., illite, chlorite, muscovite and biotite) in metamorphic rocks. Similarly, the model can also predict the preferred orientation of columnar minerals, such as tourmaline, amphibole and epidote. The model considers only isolated mineral grains and the nucleation process involves both chemical reactions and the diffusion of atoms. Thus, the nucleation of

73 quartz, calcite and olivine in quartzose, calcareous and peridotitic tectonites,

74 respectively, is not considered in this study because nucleation of these minerals

75 does not always involve significant diffusional transport.

76

77 **2. Kinetic model for nucleation**

78

79 *2.1. Nucleation under hydrostatic pressure*

80 We briefly review nucleation processes associated with the growth of new

81 mineral grains under hydrostatic pressure before considering nonhydrostatic stress

82 states.

83

84 *2.1.1. Nucleation*

85 The process of nucleation is the transformation of an embryo to a mineral

86 nucleus. A mineral embryo is an unstable phase that possesses the same physical

87 properties as the mineral itself. We consider heterogeneous nucleation (e.g., Rast,

88 1965; Spry, 1969; Shelley, 1983; Yardley, 1989; Kerrick et al., 1991; Kretz, 1994;

89 Lasaga, 1998) in our model because we focus on the nucleation of mineral species

90 that differ from surrounding, pre-existing minerals. Embryos can statistically appear

91 on any surface of pre-existing mineral grains (Fig. 1b); however, most embryos break

92 down soon after formation. Only a few successful embryos can form nuclei,

93 eventually becoming grains with measurable size through subsequent growth. The

94 details of the nucleation process remain unclear due to two challenges: the extremely

95 small size of embryos (e.g., 'a number of atoms' (Kretz, 1994, p. 300), 'around 100

96 atoms' (Smoluchouski, 1951, p. 166), or 'typically 10 to 1000 atoms' (Lasaga, 1998,

97 p. 497)) and their extraordinarily short lifespan (e.g., 'only a fraction of a second'

98 (Kretz, 1994, p. 300)). These issues prevent experimental observations of the

99 formation and breakup of embryos and the transition from embryos to nuclei.

100 To accurately discuss the nucleation of minerals, the terms 'embryo',

101 'nucleus' and 'grain' must be well defined. The definition of an embryo is clear and

102   based on energetic considerations (e.g., Kretz, 1994); however, the distinction

103   between a nucleus and a grain is ambiguous. Thus, we define these three terms with

104   respect to their size and associated Gibbs free energy (Fig. 1c). The construction of

105   the curve in Fig. 1c is explained in the online Supplementary material Appendix 1.

106

107   *2.1.2. Transition from an embryo to a nucleus*

108   We focus on the heterogeneous nucleation of a mineral on a substrate grain

109   (Fig. 1b) and assume epitaxial nucleation (e.g., Spry, 1969; Vernon, 1976; Kretz,

110   1994). During nucleation, the nucleating mineral selects a particular substrate

111   mineral and typically grows on a substrate grain with a particular orientation, which

112   minimises the interface energy between them. This process is dependent on the

113   crystallographic orientation of both minerals (e.g., Spry, 1969). Unfortunately, there

114   are no data on the crystallographic orientations of mineral pairs in the case of epitaxy

115   nucleation.

116   The compositions of metamorphic minerals are typically complex and

117   therefore their nucleation involves complicated processes. For example, muscovite

118    $(K_2Al_2[Si_6Al_2O_{20}](OH,F)_4)$ and tourmaline

119    $(Na(Mg,Fe,Mn,Li,Al)_3Al_6[Si_6O_{18}](BO_3)_3(OH,F)_4)$ (Deer et al., 1966) are each

120   composed of more than six elements. Furthermore, reactions involving phyllosilicates

121   (platy minerals) are also complex (Knipe, 1981). Thus, we aimed to develop a

122   simplified model to help with understanding natural nucleation processes. In our

123   model we do not consider stress perturbations resulting from volume changes during

124   the formation of new mineral grains or the force of crystallisation (e.g., Hobbs and

125   Ord, 2015). We assume that the rock contains numerous and variably oriented

126   substrate mineral grains prior to embryo formation. It is implicit that the surfaces of

127   substrate mineral grains are flat and their surface areas are much larger than those

128   of embryos.

129

130   *2.1.3. Nucleation rate*

131   Nucleation rate I is defined as the number of newly produced nuclei per

132   unit volume per unit time (e.g., Hollomon and Turnbull, 1953) and is typically

133   expressed as a function of absolute temperature T and hydrostatic pressure P as

134   follows:

135

136    $I(T,P) = A exp\left(-\frac{\Delta G^*}{k_B T}\right),$ (1)

137

138   Where ΔG^* is the Gibbs free energy of activation (Fig. 1c), k_B is the Boltzmann

139   constant and A is a constant (e.g., Hollomon and Turnbull, 1953; Lasaga, 1998).

140   Although P does not appear in the equation, its influence on ΔG^* is given as

141   follows:

142

143    $\Delta G^* = \Delta U^* - T\Delta S^* + P\Delta V^*,$ (2)

144

145   Where ΔU^*, ΔS^* and ΔV^* are the internal energy, entropy and volume of activation,

146   respectively (e.g., Miyashiro, 1960). ΔS^* and ΔV^* are assumed to be constant

147   under pressure–temperature conditions typical of crustal metamorphism. The validity

148   of this assumption is supported by the description of ΔV^* during diffusion by Lasaga

149   (1998). The Gibbs free energy of activation ΔG^* in Eq. (2) is a scalar property,

150   because T and P are scalar variables. Thus, ΔG^* in the present form is not

151   applicable to nucleation analysis of minerals in nonhydrostatically stressed rocks. We

152   will therefore modify this equation.

153

154   *2.2. A model of nucleation under nonhydrostatic stress*

155

156   *2.2.1. The σ_n model*

157   In our model, we replace pressure P in Eq. (2) by a normal stress term $\vec{\sigma}_n$,

158   which is applied to the nucleation site on the substrate grain. Justification for this

159   formulation is explained in the Discussion section. Normal stress ($\vec{\sigma}_n$) is a vector

160   property related to the stress field and the orientation of the nucleation site, whereas

161   the general stress field σ_{ij} is a tensor (e.g., Nadai, 1950; Timoshenko and Goodier,

162   1951; Jaeger et al., 2007). A pressure term (P) is included in our nonhydrostatic

163   stress model, following a definition of $P = (\sigma_1 + \sigma_2 + \sigma_3)/3$.

164   The Gibbs free energy of activation is represented by

165

166     $$\varDelta G^* = \Delta U^* - T\Delta S^* + \sigma_n \Delta V^*, \qquad (3)$$

167

168   Where σ_n is the magnitude of $\vec{\sigma}_n$. The nucleation rate expression in Eq. (1) is

169   consequently replaced by

170

171     $$I(T, \sigma_n) = A exp\left(-\frac{\Delta U^* - T\Delta S^* + \sigma_n \Delta V^*}{k_B T}\right). \qquad (4)$$

172

173   As the value of σ_n is dependent on the orientations in nonhydrostatically stressed

174   solids, the nucleation rate is also sensitive to variations in orientation.

175

176   *2.2.2. Stress in a Cartesian coordinate system*

177   We use principal stresses, σ_1, σ_2 and σ_3 ($\sigma_1 > \sigma_2 > \sigma_3$), compression =

178   positive) and a Cartesian coordinate system (x_1, x_2, x_3), with the coordinate axes

179   (x_1, x_2, x_3) aligned parallel to the principal stress axes (σ_1, σ_2 and σ_3) (Fig. 1d),

180   enabling simple calculations (e.g., Jaeger et al., 2007). In our analysis, we use

181   direction cosines to describe the orientation of substrate grain surfaces. The

182   orientation of a surface is provided by the direction cosines of the normal vector of

183   the plane. Figure 2a shows the angles between the normal vector and the principal

184   stress directions ϕ_1, ϕ_2 and ϕ_3, and the direction cosines l, m and n.

185   'insert Fig. 2'

186   The magnitude of the normal stress σ_n acting on a plane (e.g., Nadai,

187   1950; Jaeger et al., 2007) is given by

188

189 $\sigma_n = \sigma_1 l^2 + \sigma_2 m^2 + \sigma_3 n^2,$ (5)

190

191 with l, m and n satisfying the following equation:

192

193 $l^2 + m^2 + n^2 = 1.$ (6)

194

195 Therefore, σ_n changes with varying direction cosine values (l, m and n), reaching

196 its maximum ($\sigma_n = \sigma_1$) and minimum ($\sigma_n = \sigma_3$) values at (1, 0, 0) and (0, 0, 1),

197 respectively.

198   To simplify the analysis, we use two stress parameters $\Delta\sigma$ and ψ, defined

199 as

200

201 $\Delta\sigma = \sigma_1 - \sigma_3$ (7)

202

203 and

204

205 $\psi = \dfrac{\sigma_2 - \sigma_3}{\sigma_1 - \sigma_3}.$ (8)

206

207 Equation (8) can be rewritten as

208

209 $\sigma_2 = \psi(\sigma_1 - \sigma_3) + \sigma_3.$ (9)

210

211 *2.2.3. Formulation of nucleation rate*

212   We consider an embryo located on a flat surface of a substrate grain. As we

213 assume epitaxial nucleation, one of the crystallographic orientation axes of embryos

214 is dependent on the spatial orientation of the substrate grain, which is defined by the

215 direction cosines (l, m, n) of the normal vector to the flat surface (Fig. 2). The

216 remaining two crystallographic orientations are not considered in our model. ΔG^* of

217 Eq. (3) can be rewritten in terms of direction cosines as follows:

218

$$\Delta G^* = \Delta U^* - T\Delta S^* + (\sigma_1 l^2 + \sigma_2 m^2 + \sigma_3 n^2)\Delta V^*. \qquad (10)$$

220

221 By using the above ΔG^*, we obtain the following expression for nucleation rate:

222

$$I(T, \sigma_n) = A\exp\left[-\frac{\Delta U^* - T\Delta S^* + (\sigma_1 l^2 + \sigma_2 m^2 + \sigma_3 n^2)\Delta V^*}{k_B T}\right]. \qquad (11)$$

224

225 Thus, for a rock in a certain stress field at a given temperature, the nucleation rate is

226 expressed as

227

$$I(l, m, n) = A\exp\left(-\frac{\Delta U^*}{k_B T}\right)\exp\left(\frac{\Delta S^*}{k_B}\right)\exp\left[-\frac{(\sigma_1 l^2 + \sigma_2 m^2 + \sigma_3 n^2)\Delta V^*}{k_B T}\right]. \qquad (12)$$

229

230 As $\exp\left(-\frac{\Delta U^*}{k_B T}\right)$ and $\exp\left(\frac{\Delta S^*}{k_B}\right)$ are scalar properties independent of σ_n, they do not

231 contribute to the anisotropy of the nucleation rate. Thus, Eq. (12) can be simplified to

232

$$I(l, m, n) = A_0\exp\left[-\frac{(\sigma_1 l^2 + \sigma_2 m^2 + \sigma_3 n^2)\Delta V^*}{k_B T}\right], \qquad (13)$$

234

235 where

236

$$A_0 = A\exp\left(-\frac{\Delta U^*}{k_B T}\right)\exp\left(\frac{\Delta S^*}{k_B}\right). \qquad (14)$$

238

239 Equation (13) implicitly produces nucleation rates that are symmetrical with respect

240 to the three axes of principal stress because, for example, m and $-m$ produce the

241 same values for $I(l, m, n)$. Equation (13) is an exponential form of Lamé's stress

242 ellipsoid (e.g., Ranalli, 1995; Jaeger et al., 2007).

243

244 **3. Prediction of preferred orientations governed by nucleation**

245

246 　　　　As nucleation rate is defined as the number of newly produced nuclei per

247   unit volume per unit time, the formation of preferred orientations in rocks is controlled

248   by the orientation-dependency of the nucleation rate. Therefore, orientations

249   associated with higher nucleation rates will result in a larger number of grains. As the

250   nucleation rate is symmetrical with respect to the coordinate axes, our model obeys

251   the symmetry rule (e.g., Curie, 1894; Paterson and Weiss, 1961). Various

252   approaches have been employed to describe the preferred orientation of platy and

253   columnar minerals (see below). Using our approach, the preferred orientation

254   patterns for both columnar and platy minerals can be predicted from a single

255   nucleation rate equation (Eq. (13)) without the need for assumptions.

256   The orientation of columnar mineral grains is typically represented by the

257   orientation of grain long axes (e.g., (001) for amphibole), which commonly parallel

258   the σ_3 axis (e.g., Passchier and Trouw, 2005). Thus, for columnar minerals, ΔV^* in

259   Eq. (13) is > 0. Therefore, ΔV^* is hereafter represented by ΔV^+. The orientation of

260   platy minerals (phyllosilicates) is typically represented by poles to the basal surfaces

261   of grains (referred to crystallographically as (001); e.g., Turner and Weiss, 1963).

262   Empirical observations indicate that the basal planes of platy mineral grains are

263   typically oriented perpendicular to the σ_1 axis (e.g., Siddans, 1972; Etheridge et al.,

264   1974; Tullis, 1976; Oertel, 1985). From Eq. (13), we conclude that $\Delta V^* < 0$ for platy

265   minerals; thus, hereafter we use the symbol ΔV^-. A negative activation volume is not

266   unrealistic, because, for example, the activation volume of diffusion may be negative

267   (e.g., Lasaga, 1998). ΔV^* is reserved as a general term for activation volume,

268   including both ΔV^- and ΔV^+. Note that the signs of the activation volume for these

269   minerals are not deduced from theoretical investigations, but from previous

270   observations of naturally and experimentally deformed rocks.

271

272   *3.1. Hydrostatic stress ($\sigma_1 = \sigma_2 = \sigma_3$)*

273   Substituting $\sigma_1 = \sigma_2 = \sigma_3 = P$ into Eq.(13) we obtain

274

275   $$I(l,m,n) = A_0 \exp\left(-\frac{P\Delta V^*}{k_B T}\right). \qquad (15)$$

276

277 Therefore, Eq. (13), which was formulated for nonhydrostatic stress states, is also

278 applicable to hydrostatic stress states and predicts a random crystallographic

279 orientation of newly formed mineral grains.

280

281 *3.2. Uniaxial compression ($\sigma_1 > \sigma_2 = \sigma_3$)*

282   We now consider the uniaxial compression stress state. By substituting the

283 relation $\sigma_2 = \sigma_3$ into Eq. (13), we have

284

285 $I(l,m,n) = A_0 \exp\left[-\frac{(\sigma_1 l^2 + \sigma_3 m^2 + \sigma_3 n^2)\Delta V^*}{k_B T}\right].$ (16)

286

287 Substituting $u^2 = m^2 + n^2$, this equation becomes

288

289 $I(l,m,n) = A_0 \exp\left[-\frac{(\sigma_1 l^2 + \sigma_3 u^2)\Delta V^*}{k_B T}\right].$ (17)

290

291 As $l = \cos\phi_1$ (Fig. 2), u can be expressed as $u = \sin\phi_1$ because $l^2 + u^2 = 1$.

292 Given the following:

293

294 $\sigma_1 \cos^2\phi_1 + \sigma_3 \sin^2\phi_1 = \frac{1}{2}(\sigma_1 + \sigma_3) + \frac{1}{2}(\sigma_1 - \sigma_3)\cos2\phi_1,$ (18)

295

296 we can derive a new expression for the nucleation rate:

297

298 $I(\phi_1) = A_0 \exp\left[-\frac{(\sigma_1 \cos^2\phi_1 + \sigma_3 \sin^2\phi_1)\Delta V^*}{k_B T}\right]$

299 $\qquad = A_0 \exp\left\{-\frac{\left[\frac{1}{2}(\sigma_1 + \sigma_3) + \frac{1}{2}(\sigma_1 - \sigma_3)\cos2\phi_1\right]\Delta V^*}{k_B T}\right\}$

300 $\qquad = A_0 \exp\left[-\frac{(\sigma_1 + \sigma_3)\Delta V^*}{2k_B T}\right]\exp\left[-\frac{(\sigma_1 - \sigma_3)\cos2\phi_1 \Delta V^*}{2k_B T}\right].$ (19)

301

302 Substituting $A_{13} = A_0 \exp[-(\sigma_1 + \sigma_3)\Delta V^*/2k_B T]$ and $\Delta\sigma = \sigma_1 - \sigma_3$, we ultimately

303 derive the following equation:

304

305 $$I(\phi_1) = A_{13}\exp\left(-\frac{\Delta\sigma\Delta V^*}{2k_B T}\cos 2\phi_1\right). \qquad (20)$$

306

307 This equation represents the von Mises distribution with respect to ϕ_1, if the pre-

308 cosine term is positive (Appendix 2 in the online Supplementary material). We define

309 κ_n^+ and κ_n^- as follows:

310

311 $\kappa_n^+ = \frac{\Delta\sigma\Delta V^+}{2k_B T}$ (>0 for columnar minerals)   (21a)

312 $\kappa_n^- = \frac{\Delta\sigma\Delta V^-}{2k_B T}.$ (<0 for platy minerals)   (21b)

313

314 Thus, we designate

315

316 $I(\phi_1) = A_{13}\exp\left[\kappa_n^+\cos 2\left(\phi_1 + \frac{\pi}{2}\right)\right]$ (columnar minerals)   (22a)

317 $I(\phi_1) = A_{13}\exp(-\kappa_n^-\cos 2\phi_1).$ (platy minerals)   (22b)

318

319 The term $\pi/2$ is added to ϕ_1 in Eq. (22a) to produce a positive pre-cosine term in

320 the exponential component. Figure 3 illustrates the von Mises distributions for

321 columnar and platy minerals. The shape of the von Mises distribution depends on the

322 magnitudes of κ_n^+ and $-\kappa_n^-$, and thus on the magnitude of $\Delta\sigma$. An increase in $\Delta\sigma$

323 produces a greater difference in nucleation rate with respect to ϕ_1.

324   'insert Fig. 3'

325

326 *3.3. Uniaxial extension ($\sigma_1 = \sigma_2 > \sigma_3$)*

327   Under a uniaxial extension stress state, the nucleation rate is symmetrical

328 with respect to the σ_3 axis. Using the relation $\sigma_2 = \sigma_1$ in Eq. (13), we have

329

330    $I(l,m,n) = A_0 \exp\left[-\frac{(\sigma_1 l^2 + \sigma_1 m^2 + \sigma_3 n^2)\Delta V^*}{k_B T}\right].$ (23)

331

332   This equation becomes

333

334    $I(l,m,n) = A_0 \exp\left\{-\frac{[\sigma_1(l^2 + m^2) + \sigma_3 n^2]\Delta V^*}{k_B T}\right\},$ (24)

335

336   which is similar to that for the case of uniaxial compression. We can derive the

337   following simple equation in a similar manner by noting that $\cos\phi_3 = n$ (Fig. 2a) and

338    $\sin\phi_3 = \sqrt{l^2 + m^2}$:

339

340    $I(\phi_3) = A_0 \exp\left[-\frac{(\sigma_1 + \sigma_3)\Delta V^*}{2k_B T}\right] \exp\left[-\frac{\Delta\sigma\Delta V^*}{2k_B T}\cos 2\phi_3\right].$ (25)

341

342   Using $A_{13} = A_0 \exp[-(\sigma_1 + \sigma_3)\Delta V^*/2k_B T]$ and the κ_n^+ and κ_n^- terms in Eq. (21), this

343   equation is simplified to

344

345    $I(\phi_3) = A_{13}\exp(\kappa_n^+ \cos 2\phi_3)$ (columnar minerals)   (26a)

346    $I(\phi_3) = A_{13}\exp\left[-\kappa_n^- \cos 2\left(\phi_3 + \frac{\pi}{2}\right)\right].$ (platy minerals)   (26b)

347

348   These equations represent von Mises distributions with respect to ϕ_3 (Appendix 2 in

349   the online Supplementary material).

350

351   *3.4 General triaxial stress ($\sigma_1 > \sigma_2 > \sigma_3$)*

352   To simplify our analysis, we focus on the value of σ_2. When σ_2 approaches

353   σ_3 or σ_1, nucleation rate distributions approach those of uniaxial compression or

354   extension, respectively. Thus, the characteristics of nucleation under triaxial stress

355   are influenced by the magnitude of σ_2 relative to σ_1 and σ_3. The parameter ψ,

356   defined as $(\sigma_2 - \sigma_3)/(\sigma_1 - \sigma_3)$ in Eq. (8), can be used to describe stress states: ψ

357   is 0 for uniaxial compression, 1 for uniaxial extension, and between 0 and 1 for

358   triaxial stress states. The following analysis includes the cases of uniaxial extension

359   and compression. We can depict nucleation-rate profiles for three sections (Table 1):

360    $x_1 - x_2$, $x_2 - x_3$ and $x_3 - x_1$ as follows.

361   'insert Table 1'

362

363   *3.4.1.* Section $x_1 - x_2$ *(n = 0)*

364   The nucleation-rate profile for section $x_1 - x_2$ can be depicted by

365   substituting $n = 0$ into Eq. (13), which then becomes

366

367    $I(\phi_1) = A_3\exp\left[(1 - \psi)\kappa_n^+ \cos2\left(\phi_1 + \frac{\pi}{2}\right)\right]$ (columnar minerals)   (27a)

368    $I(\phi_1) = A_3\exp[(\psi - 1)\kappa_n^- \cos2\phi_1]$.   (platy minerals)   (27b)

369

370   The derivations of Eq. (27) and A_3 are provided in the online Supplementary

371   material Appendix A3.1. These equations represent von Mises distributions with

372   respect to ϕ_1.

373

374   *3.4.2.* Section $x_2 - x_3$ *(l = 0)*

375   The nucleation-rate profile for section $x_2 - x_3$ can be depicted by substituting

376    $l = 0$ into Eq. (13), which then becomes

377

378    $I(\phi_3) = A_1\exp(\psi\kappa_n^+ \cos2\phi_3)$ (columnar minerals)   (28a)

379    $I(\phi_3) = A_1\exp\left[-\psi\kappa_n^- \cos2\left(\phi_3 + \frac{\pi}{2}\right)\right]$.   (platy minerals)   (28b)

380

381   The derivations of Eq. (28) and A_1 are provided in the online Supplementary

382   material Appendix A3.2. In these equations, we use $\cos\phi_3 = n$ (Fig. 2a). These

383   equations represent von Mises distributions with respect to ϕ_3.

384

385   *3.4.3.* Section $x_3 - x_1$ *(m = 0)*

386   Nucleation-rate profiles for section $x_3 - x_1$ can be depicted by substituting

387     $m = 0$ into Eq. (13), which then becomes

388

389     $I(\phi_1) = A_{13}\exp\left[\kappa_n^+ \cos 2\left(\phi_1 + \frac{\pi}{2}\right)\right]$ (columnar minerals)   (29a)

390     $I(\phi_1) = A_{13}\exp(-\kappa_n^- \cos 2\phi_1).$ (platy minerals)   (29b)

391

392   The derivations of these equations and A_{13} are provided in the online

393   Supplementary material Appendix A3.3. These equations represent von Mises

394   distributions with respect to ϕ_1.

395

396   *3.5. Stereographic projection*

397   Here, we produce contoured stereographic projection diagrams showing

398   nucleation rates for all stress states. As before, we progress from Eq. (13). To avoid

399   confusion, we deal with columnar and platy minerals separately due to the

400   differences in the signs of their activation volumes.

401

402   *3.5.1. Columnar minerals ($\Delta V^+ > 0$)*

403   The maximum nucleation rate is attained at direction cosines of (0, 0, 1),

404   with the rate given by

405

406     $I(0,0,1) = A_0 \exp\left(-\frac{\sigma_3 \Delta V^+}{k_B T}\right).$ (30)

407

408   We designate a constant d $(0 < d < 1)$ to derive a nucleation rate that is

409   proportional to the maximum nucleation rate, as follows:

410

411     $d = \dfrac{I(l,m,n)}{I(0,0,1)} = \dfrac{A_0 \exp\left[-\frac{(\sigma_1 l^2 + \sigma_2 m^2 + \sigma_3 n^2)\Delta V^+}{k_B T}\right]}{A_0 \exp\left(-\frac{\sigma_3 \Delta V^+}{k_B T}\right)}.$ (31)

412

413   This equation can then be transformed to

414

415 $$d = \exp\left[-\frac{(\sigma_1 l^2 + \sigma_2 m^2 + \sigma_3 n^2 - \sigma_3)\Delta V^+}{k_B T}\right]. \qquad (32)$$

416

417   For our analysis we use an equal-area upper-hemisphere stereographic

418 projection (Schmidt net; Fig. 2c and Appendix 4 in the online Supplementary

419 material). The $\sigma_1 - \sigma_3$ plane is represented by the perimeter of the diagram and

420 σ_2 is located at the centre of the net (Fig. 2c). The positions of points on the

421 stereographic net are determined by two angles: the azimuthal angle to the σ_1 axis

422 (α) and the vertical angle from the $\sigma_1 - \sigma_3$ surface (β). The direction cosines

423 (l, m, n) are expressed in terms of the stereographic angles α and β as $l =$

424 $\cos\alpha\cos\beta$, $m = \sin\beta$ and $n = \sin\alpha\cos\beta$, respectively.

425   The angles of the stereographic projection (Fig. 2c) are related as follows:

426

427 $$\frac{\ln(1/d)}{2\kappa_n^+} - \psi = (\cos^2\alpha - \psi)\cos^2\beta, \qquad (33)$$

428

429 which is derived in the online Supplementary material Appendix A5.1. This equation

430 gives α as a function of β, and such (α, β) pairs are used to generate contours for

431 each d value. Similarly, other pairs such as $(\alpha, -\beta)$, $(-\alpha, \beta)$ and $(-\alpha, -\beta)$ also

432 constitute contour lines. We draw contour diagrams by using this equation with d

433 values of 0.1–0.9, with an interval of 0.1, and forcing the terms on the left to be >0

434 (Fig. 4). The value for d needs to be chosen carefully, as it must satisfy

435

436 $$d\exp\left(-\frac{\sigma_3 \Delta V^+}{k_B T}\right) \geq \exp\left(-\frac{\sigma_1 \Delta V^+}{k_B T}\right). \qquad (34)$$

437

438   'insert Fig. 4'

439 *3.5.2. Platy minerals ($\Delta V^- < 0$)*

440   The maximum nucleation rate for platy minerals is attained at (1, 0, 0), with

441 the rate given by

442

443 $$I(1,0,0) = A_0 \exp\left(-\frac{\sigma_1 \Delta V^-}{k_B T}\right). \qquad (35)$$

444

445　We designate a constant d $(0 < d < 1)$ to derive a nucleation rate proportional to

446　the maximum nucleation rate, as follows:

447

448　$$d = \frac{I(l,m,n)}{I(1,0,0)} = \frac{A_0\exp\left[-\frac{(\sigma_1 l^2 + \sigma_2 m^2 + \sigma_3 n^2)\Delta V^-}{k_B T}\right]}{A_0\exp\left(-\frac{\sigma_1 \Delta V^-}{k_B T}\right)}. \qquad (36)$$

449

450　This equation is transformed to

451

452　$$d = \exp\left[\frac{(\sigma_1 - \sigma_1 l^2 - \sigma_2 m^2 - \sigma_3 n^2)\Delta V^-}{k_B T}\right]. \qquad (37)$$

453

454　The orientation (l, m, n) can be expressed in terms of α and β angles as

455　$(\cos\alpha\cos\beta, \sin\beta, \sin\alpha\cos\beta)$. By eliminating l, m and n from Eq. (37), we obtain

456

457　$$(\psi - \cos^2\alpha)\cos^2\beta = \frac{\ln d}{2\kappa_n^-} + (\psi - 1), \qquad (38)$$

458

459　which is derived in the online Supplementary material Appendix A5.2. This equation

460　also gives (α, β), $(\alpha, -\beta)$, $(-\alpha, \beta)$ and $(-\alpha, -\beta)$ pairs for a given d-value. The

461　value for d must satisfy the following:

462

463　$$d\exp\left(-\frac{\sigma_1 \Delta V^-}{k_B T}\right) \geq \exp\left(-\frac{\sigma_3 \Delta V^-}{k_B T}\right). \qquad (39)$$

464

465　The results are illustrated in Fig. 5. In addition, we constructed nucleation contour

466　diagrams with σ_1 at the centre of the net (Fig. 6) by rotating the σ_1 and σ_2 axes by

467　90°. The method for such rotations is described by Turner and Weiss (1963).

468　　　　　　　　　　　　　　　　　　　　　　　　　　　　　　　　'insert Fig. 5'

469　　　　　　　　　　　　　　　　　　　　　　　　　　　　　　　　'insert Fig. 6'

470

471　*3.6. Contoured nucleation-rate diagrams for triaxial stress states*

472   Nucleation rate is controlled by an exponential form of the Lamé's stress

473   ellipsoid. For both columnar and platy minerals, the shape of the Schmidt net fabric

474   diagram changes as the values $\kappa_n^{\pm}$ (κ_n^{+} and κ_n^{-}) and ψ are varied (Figs 4–6). The

475   strength of the preferred orientation is enhanced by an increasing absolute value of

476    $\kappa_n^{\pm}$. An increase in ψ, from uniaxial compression ($\psi = 0$) to uniaxial extension ($\psi =$

477   1), will alter the symmetry of the contours; i.e., columnar minerals exhibit a change

478   from girdle to point-maximum patterns, whereas platy minerals change from point-

479   maximum to girdle patterns. These variations are similar to those theoretically

480   predicted by Woodcock (1977, fig. 3), Shelley (1983, fig. 7.30 for amphibole and fig.

481   7.11 for platy minerals), and Sintubin (1998, fig. 1A for mica), which were based on

482   the symmetry of stress and/or strain fields.

483   'insert Fig. 7'

484

485   **4. Discussion**

486

487   *4.1. Examples of preferred orientations in metamorphic rocks*

488   Nucleation rate (I) is proportional to the number of newly nucleated grains in

489   a given volume per unit time. Thus, nucleation rate with respect to orientation reflects

490   the preferred orientation of mineral grains. To determine the applicability of our

491   model, we analysed previously published 2D and 3D orientation data for columnar

492   and platy minerals, plotted on Schmidt net fabric diagrams. Although some data are

493   dissimilar to our model predictions, we also identify many data that are consistent

494   with our predictions, indicating that our model may be useful for the analysis of

495   preferred orientations in natural rocks.

496

497   *4.1.1. Columnar minerals*

498   Shape-preferred orientation data for columnar minerals (i.e., the

499   concentration of long axes relative to the foliation surface) have been reported by

500   Masuda et al. (1999, 2004, 2008, 2011) and Omori et al. (2016). These authors

501   analysed glaucophane, tourmaline and piemontite in metachert and marble from

502   high-pressure metamorphic belts and a metamorphic sole. The samples contained

503   no microfolds. Figure 7 shows four representative examples of orientation distribution

504   diagrams for samples from Greece and Turkey (Masuda et al., 2004, 2008, 2011).

505   The orientation distributions in these examples fit well with the von Mises distribution

506   at various κ values.

507   Pole-figure diagrams for columnar minerals have been widely published

508   (e.g., Sander, 1930; Turner and Weiss, 1963) and two examples are shown in Fig. 8a

509   and c, with two corresponding contour diagrams predicted by the model presented in

510   Fig. 8b and d. The figure pairs (8a–b and 8c–d) appear relatively similar. However, It

511   should be noted that the model diagrams were constructed using a different

512   contouring method than that for typical fabric diagrams. In most fabric diagrams, the

513   contours have a spacing of >1 (Fig. 8a and b), whereas our model uses a spacing of

514   ≤ 1 (Fig. 8b and d).

515   'insert Fig. 8'

516

517   *4.1.2. Platy minerals*

518   Two-dimensional orientation data for platy minerals are rare compared with

519   stereographic projection data (see below), and we focus on two examples. Bell

520   (1979) presented two generations of biotite in a single diagram, producing

521   histograms with peaks at orientations parallel to the foliation and bedding (Fig. 9a).

522   We tentatively fit the distribution of mica grains around the foliation using the von

523   Mises distribution, which appears to generate an acceptable result. Two-dimensional

524   analysis is particularly useful if the sample contains a mixture of phyllosilicate grains

525   with distinct origins. Mancktelow (1979) used an optical microscope to identify

526   internal deformation features such as kink bands and undulatory extinction, which

527   were used to discriminate between two generations of biotite (plotted as two

528   histograms; Fig. 9b). The von Mises distribution fits orientation data for the younger

529   generation of biotite ($\kappa = -57$), whereas it does not fit the orientation data for the

530 older grains.

531 'insert Fig. 9'

532 Preferred orientation data (plotted on Schmidt nets) for platy minerals in

533 slates, phyllites, schists and gneisses have been acquired for more than 90 years

534 (e.g., Schmidt, 1925; Sander, 1930; Knopf and Ingerson, 1937; Fairbairn, 1949,

535 Turner and Weiss, 1963; Wenk, 1985). Among such data, we select four examples

536 displaying distinct orientation distributions, irrespective of the genetic interpretation of

537 the authors (Fig. 10). These preferred-orientation patterns are presented as

538 contoured equal-area (Schmidt net) lower-hemisphere diagrams showing the

539 orientations of poles to the basal surfaces (001) of grains.

540 'insert Fig. 10'

541 Muscovite data of Wenk et al. (2018; Fig. 10a) display a high concentration

542 of orientations perpendicular to the foliation surface, similar to the predicted pattern

543 at $\psi = 0$ and $\kappa_n^- = -14$ (Fig. 10b). The elliptical orientation distribution of mica

544 grains described by Oertel and Phakey (1972; Fig. 10c) is consistent with the

545 predicted pattern at $\psi = 0.5$ and $\kappa_n^- = -4$ (Fig. 10d); however, the orientations of

546 the long axes of the ellipses differ between the two diagrams due to a difference in

547 reference frame in the Schmidt nets. Furthermore, muscovite orientation data of

548 Holeywell and Tullis (1975; Fig. 10e) are similar to the model pattern at $\psi = 0.8$ and

549 $\kappa_n^- = -2.5$ (Fig. 10f). Chlorite data reported by Ishii (1988; Fig. 10g) are also

550 consistent with the model, at values of $\psi = 0.9$ and $\kappa_n^- = -0.55$ (Fig. 10h). These

551 four examples correspond to almost the full range of ψ values, from 0 to 0.9, and a

552 wide range of κ_n^- values, from –0.55 to –14.

553

554 *4.1.3. Evaluating the applicability of the model*

555 The fitting of selected data with the predicted orientation patterns appears

556 excellent (Figs 7–10). As nucleation is not an instantaneous process in natural rocks,

557 but rather an enduring one that occurs during changing temperature and pressure

558 conditions (e.g., Ridley, 1985), grains observed in a rock would have undergone

559 diachronous nucleation. The good fit between model and natural orientation

560 distributions suggests that nucleation occurred over a short time, during which $\Delta\sigma$

561 and ψ did not vary significantly.

562   The good fit of the model does not necessarily indicate that it is valid, given

563 the possibility of alternative interpretations. At least six processes are known to

564 generate preferred orientations of minerals: nucleation, growth, Ostwald ripening,

565 plastic deformation (including dislocation glide and kinking), rigid-body rotation and

566 pressure solution (e.g., Passchier and Trouw, 2005; Twiss and Moores, 2007). Some

567 of these processes may operate simultaneously in nonhydrostatically stressed

568 metamorphic rocks. Our model considers only nucleation, whereas natural preferred

569 orientations will be affected by all of the above-mentioned processes. Therefore,

570 more studies are required to determine the origin of preferred orientations in

571 metamorphic tectonites.

572

573 *4.2. Atomistic model for the formation of embryos under nonhydrostatic stress*

574   On the basis of schematic diagrams (e.g. figs. 75 and 85 of Buckley, 1951;

575 fig. 7.45 of Lasaga, 1998) we speculate that mineral embryos form from atoms and

576 unit cells via the following three steps (Fig. 11).

577

578 *4.2.1. Step 1: formation of a unit cell on a substrate grain (Fig. 11a)*

579   We consider the case in which a nucleating mineral forms unit cells on a

580 substrate mineral grain. The shape of the unit cell is represented by a rectangle in

581 Fig. 11 and the length of the substrate grain is exaggerated. Individual and bonded

582 atoms encounter the substrate grain via diffusion through the rock and will form new

583 unit cells of the nucleating mineral by integrating with other atoms on the surface of

584 the substrate grain. Some unit cells form at unfavourable orientations with respect to

585 the substrate grain (Fig. 11a, second unit cell from the left) and soon break down and

586 reconstruct to form new unit cells with more favourable orientations. Unit cells may

587 also form by chance, far from substrate grains. Such cells are unlikely to migrate to

588 the surface of the substrate grain due to their high probability of breaking down and

589 the sluggishness of their diffusion through solids.

590   'insert Fig. 11'

591

592 *4.2.2. Step 2: formation of a single-layer embryo (Fig. 11b)*

593   Isolated unit cells on substrate grain surfaces are unstable and will

594 eventually break down to individual atoms. Unit cells may move laterally along the

595 surface of the substrate grain, maintaining their structure. When they encounter other

596 unit cells, they bind together to form a single-layer embryo, which is more stable than

597 isolated unit cells. A single-layer embryo can be enlarged through the addition of

598 atoms (and/or unit cells) along its margin. As the movement rate of isolated atoms

599 and groups of atoms along the surface of the substrate grain is much higher than that

600 of unit cells, enlargement via the addition of atoms is likely the dominant process.

601 The number of atoms that land on the top surface of the single-layer embryo is

602 negligibly small owing to the small area of the surface. Therefore, unit cells are

603 unlikely to be produced on the top surfaces of single-layer embryos.

604

605 *4.2.3. Step 3: construction of a multi-layer embryo (Fig. 11c)*

606   A single-layer embryo remains unstable and will eventually break down,

607 whereas multi-layer embryos are more stable due to their lower surface-to-volume

608 ratios (see Appendix 1 in the online Supplementary material). Therefore, a single-

609 layer embryo must become a multi-layer embryo to survive long enough to transform

610 into a nucleus. To form a multi-layer embryo, unit cells on the surface of the substrate

611 grain must climb onto the top of the embryo, under the influence of normal stress.

612   Isolated or groups of atoms may land on the upper surface of the single-

613 layer embryo. However, in such cases, unit cells are unlikely to be produced due to

614 the lack of partner atoms of the nucleating mineral. As the surface area of single-

615 layer embryos is very small compared with that of the substrate grain, unit cells

616 formed through such processes are likely very rare and negligibly small in number.

617

4.2.4. Note on the formation of nuclei

As σ_n differs with respect to the orientation of the surface under nonhydrostatic stress states, the nucleation rate also differs. Our model indicates that thickening of embryos is a vital step in nucleation and that the rate-controlling process is the climbing of unit cells under the influence of σ_n (step 3). Therefore, the magnitude of σ_n controls all nucleation processes. A positive activation volume indicates that normal stress will restrict nuclei formation, whereas a negative activation volume indicates that normal stress accelerates the process. Here, we are referring to the activation volume of a transitional phase, rather than that of a stable mineral. We simply regard activation volume as a specific constant that characterises the influence of pressure on the material and do not discuss its physical meaning. Furthermore, the transition states of columnar and platy minerals remain generally unconstrained.

5. Conclusion

We present a kinetic model for the anisotropic nucleation rate of minerals in nonhydrostatically stressed metamorphic rocks. The model can quantitatively predict development of the preferred orientation of columnar and platy minerals in terms of $\kappa_n^{\pm}$ (the concentration parameter of the von Mises distribution defined by $\Delta\sigma\Delta V^*/2k_BT$) and ψ (the stress parameter defined by $(\sigma_2 - \sigma_3)/(\sigma_1 - \sigma_3)$). As the model only considers mineral nucleation, it cannot always be applied to the preferred orientation of minerals in naturally deformed rocks. The model will contribute to our understanding of how minerals develop a preferred orientation in deformed rocks.

655

656

657   **On line Supplementary material**

658   Appendix 1. Gibbs free energy of activation during nucleation

659   Appendix 2. The von Mises distribution

660   Appendix 3. Derivation of nucleation-rate equations

661   Appendix 4. Direction cosines and stereographic projection

662   Appendix 5. Contours on stereographic projection

663

664

665   **References**

666

667   Bell, T.H., 1978. The development of slaty cleavage across the Nackara arc of the

668   Adelaide geosyncline. Tectonophysics 51, 171–202.

669

670   Buckley, H.E., 1951. Crystal Growth. John Wiley & Sons, London.

671

672   Curie, P., 1894. Sur la symétrie dans les phénomènas physique, symétrie d'un

673   champ électrique et d'un champ magnétique. Journal de Physique 3, 393–415.

674

675 Deer, W.A., Howie, R.A., Zussman, J., 1966. An Introduction to the Rock Forming

676 Minerals. Longman, London.

677

678 Etheridge, M.A., Paterson, M.S., Hobbs, B.E., 1974. Experimentally produced

679 preferred orientation in synthetic mica aggregates. Contributions to Mineralogy and

680 Petrology 44, 275–294.

681

682 Fairbairn, H.W., 1949. Structural Petrology of Deformed Rocks. Cambridge, Addison

683 Wesley.

684

685 Fisher, N.I., 1993. Statistical Analysis of Circular Data. Cambridge University Press,

686 Cambridge.

687

688 Hobbs, B., Ord, A., 2015. Structural Geology: The Mechanics of Deforming

689 Metamorphic Rocks, volume 1: Principles. Elsevier, Amsterdam.

690

691 Hobbs, B.E., Means, W.D., Williams, P.F., 1976. An Outline of Structural Geology.

692 John Wiley & Sons, New York.

693

694 Hollomon, J.H., Turnbull, D., 1953. Nucleation. Progress in Metal Physics 4, 333–

695 388.

696

697 Holeywell, R.C., Tullis, T.E., 1975. Mineral reorientation and slaty cleavage in the

698 Martinsburg formation, Lehigh Gap, Pennsylvania. Geological Society of America

699 Bulletin 86, 1296–1304.

700

701 Ishii, K., 1988. Grain growth and re-orientation of phyllosilicate minerals during the

702 development of slaty cleavage in the South Kitakami Mountains, northeast Japan.

703 Journal of Structural Geology 10, 145–154.

704

705 Jaeger, J.C., Cook, N.G.W., Zimmerman, R.W., 2007. Fundamentals of Rock

706 Mechanics, 4th ed. Blackwell, Malden.

707

708 Kamb, W.B., 1959, Theory of preferred orientation developed by crystallization under

709 stress. Journal of Geology 67, 153–170.

710

711 Keppler, R., Ullemeyer, K., Behrmann, J.H., Stipp, M., Kurzawski, R.M., Lokajíček, T.,

712 2015. Crystallographic preferred orientations of exhumed subduction channel rocks

713 from the Eclogite Zone of the Tauern Window (Eastern Alps, Austria), and

714 Implications on rock elastic anisotropies at great depth. Tectonophysics 647–648,

715 89–104.

716

717 Kerrick, D.M., Lasaga, A.C., Raeburn, S.P., 1991. Kinetics of heterogeneous

718 reactions. In: Kerrick, D.M. (ed.), Contact Metamorphism. Reviews in Mineralogy 26,

719 583–671.

720

721 Knipe, R.J., 1981. The interaction of deformation and metamorphism in slates.

722 Tectonophysics 78, 240–272.

723

724 Knopf, E.B., Ingerson, E., 1938. Structural Petrology. Geological Society of America

725 Memoir 6.

726

727 Kretz, R., 1994. Metamorphic Crystallization. John Wiley & Sons, Chichester.

728

729 Kumazawa, M., 1963. A fundamental thermodynamic theory on nonhydrostatic field

730 and on the stability of mineral orientation and phase equilibrium. Journal of Earth

731 Science Nagoya University 11, 145–217.

732

733   Lasaga, A.C., 1998. Kinetic Theory in the Earth Sciences. Princeton University Press,

734   Princeton.

735

736   Mancktelow, N.S., 1979. The development of slaty cleavage, Fleurieu Peninsula,

737   South Australia. In: Bell, T.H., Vernon, R.H. (eds.), Microstructural Processes during

738   Deformation and Metamorphism. Tectonophysics 58, 1–20.

739

740   Mardia, K.V., 1972. Statistics of Directional Data. Academic Press, London.

741

742   Masuda, T., Kugimiya, Y., Aoshima, I., Hara, Y., Ikei, H., 1999. A statistical approach to

743   determination of a mineral lineation. Journal of Structural Geology 21, 467-472.

744

745   Masuda, T., Miyake, T., Kimura, N., Okamoto, A., 2011. Application of the microboudin

746   method to palaeodifferential stress analysis of deformed impure marbles from Syros,

747   Greece: implications for grain-size and calcite-twin palaeopiezometers. Journal of

748   Structural Geology 33, 20-31.

749

750   Masuda, T., Nakayama, S., Kimura, N., Onodera, K., Okamoto, A., 2004. Triaxial stress

751   state deep in orogenic belts: an example from Turkey. Journal of Structural Geology

752   26, 2203-2209.

753

754   Masuda, T., Nakayama, S., Kimura, N., Okamoto, A., 2008. Magnitude of σ_1, σ_2 and

755   σ_3 at mid-crustal levels in the continental crust: microboudin method applied to an

756   impure metachert from Turkey. Tectonophysics 460, 230-236.

757

758   Miyashiro, A., 1960. Thermodynamics of Rocks and Minerals. Chidanken, Tokyo. (in

759   Japanese)

760

761   Nadai, A., 1950. Theory of Flow and Fracture of Solids. McGraw-Hill, New York.

762

763 Oertel, G., 1985. Phyllosilicate textures in slates. In: Wenk, H.-R. (ed.), Preferred

764 Orientation in Deformed Metals and Rocks: an Introduction to Modern Texture

765 Analysis. Academic Press, Orlando, 431–440.

766

767 Oertel, G., Phakey, F., 1972. The texture of a slate from Nantlle, Caernarvon, North

768 Wales. Texture 1, 1–8.

769

770 Omori, Y., Barresi, A., Kimura, N., Okamoto, A., Masuda, T., 2016. Contrast in stress–

771 strain history during exhumation between high- and ultrahigh-pressure metamorphic

772 units in the Western Alps: microboudinage analysis of piemontite in metacherts.

773 Journal of Structural Geology 89, 168–180.

774

775 Passchier, C.W., Trouw, R.A.J., 2005. Microtectonics, 2nd ed. Springer, Berlin.

776

777 Paterson, M.S., 1973. Nonhydrostatic thermodynamics and its geological

778 applications. Review of Geophysics and Space Physics 11, 355–389.

779

780 Paterson, M.S., Weiss, L.E., 1961. Symmetry concepts in the structural analysis of

781 deformed rocks. Geological Society of America Bulletin, **72**, 841–882.

782

783 Putnis, A., McConnell, J.D.C., 1980. Principles of Mineral Behaviour. Blackwell,

784 Oxford.

785

786 Ranalli, G., 1995. Rheology of the Earth. Chapman & Hall, London.

787

788 Rast, N., 1965. Nucleation and growth of metamorphic minerals. In: Pitcher, W.S.,

789 Flinn, G.W. (eds.), Controls of Metamorphism, Oliver & Boyd, Edinburgh and London,

790 pp. 73–102.

791

792   Ridley, J., 1985. The effect of reaction enthalpy on the progress of a metamorphic

793   reaction. In: Thompson, A.B., Rubie, D.C. (eds.), Advances in Physical Geochemistry,

794   Vol. 4, Springer-Verlag, New York, 80–97.

795

796   Rousell, D.H., 1981. Fabric and origin of gneissic layers in anorthositic rocks of the

797   St. Charles sill, Ontario. Canadian Journal of Earth Science, 18, 1681–1693.

798

799   Sander, B., 1930. Gefügekunde der Gesteine. Springer, Vienna.

800

801   Schmidt, W., 1925. Gefügestatistik. Tschermaks mineralogische und petrographische

802   Mitteilungen 38, 395–399.

803

804   Shelley, D., 1983. Igneous and Metamorphic Rocks under the Microscope. Chapman

805   & Hall, London.

806

807   Siddans, A.W.B., 1972. Slaty cleavage – a review of research since 1815. Earth-

808   Science Review, 8, 205–232.

809

810   Sintubin, M., 1998. Mica (110) pole figures in support of Marchian behavior of

811   phyllosilicates during the development of phyllosilicate preferred orientation.

812   Materials Science Forum, 273–275, 601–606.

813

814   Smoluchowski, R., 1951. Nucleation theory. In Phase Transitions in Solids,

815   Smoluchowski, R., Mayer, J.E., Weyl, W.A. (ed.), 149–182, John Wiley & Sons, New

816   York and Chapman & Hall, London.

817

818   Spear, F.S., 1993. Metamorphic Phase Equilibria and Pressure-Temperature-Time

819   Paths. Mineralogical Society of America, Washington.

Spry, A. 1969. Metamorphic Textures. Pergamon Press, Oxford.

Terasawa, K., 1960. Sugaku-gairon. Iwanami, Tokyo. (Textbook on Mathematics written in Japanese)

Timoshenko, S.P., Goodier, J.N., 1951. Theory of Elasticity, 2nd ed. McGraw-Hill, New York.

Tullis, T.E., 1976. Experiments on the origin of slaty cleavage and schistosity. Bulletin of Geological Society of America, 87, 745–753.

Turner, F.J., Weiss, L.E., 1963. Structural Analysis of Metamorphic Tectonites. McGraw Hill, New York.

Twiss, R.J., Moores, E.M., 2007. Structural Geology, 2nd ed. W.H. Freeman and Company, New York.

Vernon, R.H., 1976. Metamorphic Processes. George Allen & Unwin Ltd., London.

Vernon, R.H., 2004. A Practical Guide to Rock Microstructure. Cambridge University Press, Cambridge.

Vernon, R.H., Clarke, G.L., 2008. Principles of Metamorphic Petrology. Cambridge University Press, Cambridge.

von Mises, R., 1918. Über die "Ganzzahligkeit" der Atomgewichte und Verwandte Fragen. Physikal Zeitschrift 19, 490–500.

849   Wenk, H.-R., 1985. Preferred Orientation in Deformed Metals and Rocks: an

850   Introduction to Modern Texture Analysis. Academic Press, Orlando,

851

852   Wenk, H.-R., Kanipanyacharoen, W., Ren, Y., 2018. Slate – A new record for crystal

853   preferred orientation. Journal of Structural Geology, 125, 319–324.

854

855   Woodcock, N.H., 1977. Specification of fabric shapes using an eigenvalue method.

856   Geological Society of America Bulletin, 88, 1231–1236.

857

858   Yardley, B.W.D., 1989. An Introduction to Metamorphic Petrology. Longman, Essex.

859

860 **Figure captions**

861

862 Fig. 1. Model framework. (a) Schematic diagram illustrating the difference in Gibbs

863   free energy (ΔG) between reactants (initial state) and products (final state) with

864   respect to the reaction coordinate (modified after fig. 4.2 of Putnis and

865   McConnell, 1980). ΔG^*: Gibbs free energy of activation. (b) Schematic diagram

866   showing embryos of columnar and platy minerals during heterogeneous

867   nucleation. Embryos (dark grey) form on flat surfaces of substrate grains (light

868   grey). The shapes of the embryos are controlled by their crystal habit. For

869   simplicity, the long axis of columnar minerals is assumed to be perpendicular to

870   the surface of substrate grains. $\vec{\sigma}_n$ is the stress vector operating perpendicular

871   to each flat surface of the substrate grain. The substrate grains and embryos

872   are surrounded by a stress-transmittable material (not shown). (c) Schematic

873   energy profile for a range of crystalline particles, from embryos through nuclei,

874   to grains (modified after Putnis and McConnell, 1980 and Kretz, 1994). Particle

875   size reflects the number of constituent atoms. The distinction between nucleus

876   and grain is tentatively made based on the magnitude of Gibbs free energy. (d)

877   The Cartesian coordinate system in nonhydrostatically stressed metamorphic

878   rocks. Coordinate axes (x_1, x_2 and x_3) are oriented parallel to the principal

879   stress axes (σ_1, σ_2 and σ_3).

880

881 Fig. 2. Direction cosines and stereographic projection. (a) Direction cosine angles

882   (ϕ_1, ϕ_2 and ϕ_3) for a pole to a substrate grain surface (dark grey). The thick

883   line intersecting the origin is oriented perpendicular to the mineral surface. (b)

884   Angles used for the construction of upper-hemisphere stereographic projections

885   (α and β). (c) Upper-hemisphere stereographic projection. σ_1, σ_2 and σ_3 are

886   located in the centre, at the top and bottom, and on the left and right of the

887   diagram, respectively. The horizontal and vertical lines designate the $\sigma_2 - \sigma_3$

888   and $\sigma_1 - \sigma_2$ planes, respectively.

889

Fig. 3. Profile of representative von Mises distributions (f) with respect to a dummy
angle (θ) with a mode at 90°, at which the distributions are at a maximum.
Annotated numbers indicate the concentration parameter κ for each
distribution. The concentration of orientations becomes greater with increasing
κ. κ is not equivalent to κ_n^+ or $-\kappa_n^-$, and depends on the orientation of the
section and mineral grain. See Table 1 for the relationships among κ, κ_n^+ or
$-\kappa_n^-$.

897

Fig. 4. Predicted contour diagrams (Schmidt nets) for the nucleation rate of columnar
minerals in terms of κ_n^+ and ψ. The positions of σ_1, σ_2 and σ_3 in the
diagrams are indicated in Fig. 2c. The horizontal line through the centre of each
diagram represents a plane perpendicular to σ_1, and the centre corresponds to
σ_2. The maximum nucleation rate ($d = 1$) is attained at σ_3. The coloured
contour lines correspond to d values from 0.1 to 1, with an interval of 0.1. The
red horizontal line ($\psi = 0$) and red points (exaggerated in scale) at both ends of
the black horizontal line ($0 < \psi \leq 1$) represent $d = 1$. The black line indicates
$d = 0.5$.

907

Fig. 5. Predicted contour diagrams (Schmidt net) for the nucleation rate of platy
minerals in terms of $-\kappa_n^-$ and ψ. Note that a negative sign (−) is attached to
κ_n^- because $\kappa_n^- < 0$. The positions of σ_1, σ_2 and σ_3 in the diagrams are
indicated in Fig. 2c. The horizontal line through the centre of each diagram
represents a plane perpendicular to σ_1, and the centre corresponds to σ_2. The
maximum nucleation rate ($d = 1$) is attained at σ_1. The coloured contour lines
correspond to d values from 0.1 to 1, with an interval of 0.1. The red line ($\psi = 1$) and red points ($\psi < 1$) represent $d = 1$. The black line represents $d = 0.5$.

916

917   Fig. 6. Predicted contour diagrams (Schmidt net) for the nucleation rate of platy

918   minerals in terms of $-\kappa_n^-$ and ψ. A negative sign (−) is attached to κ_n^-

919   because $\kappa_n^- < 0$. The centre of the diagram corresponds to σ_1, and the top and

920   bottom represent σ_2. Note that the positions of σ_1 and σ_2 are different from

921   those in Fig. 5. The coloured contour lines correspond to d values from 0.1 to

922   1, with an interval of 0.1. The maximum nucleation rate ($d = 1$) is attained at the

923   centre of the diagram (red point; $\psi < 1$) and along the red line ($\psi = 1$). The

924   black line indicates $d = 0.5$.

925

926   Fig. 7. Examples of 2D shape-preferred orientations of columnar minerals. (a)

927   Glaucophane in marble from Delfini, Syros, Greece; from fig. 3(a) of Masuda et

928   al. (2011). (b) Tourmaline in metachert from Eskisehir, Turkey; from fig. 1 of

929   Masuda et al. (2008). (c) Glaucophane in metachert from Eskisehir, Turkey;

930   from fig. 3 of Masuda et al. (2004). (d) Glaucophane in marble from Kampos,

931   Syros, Greece; from fig. 3(b) of Masuda et al. (2011). Measurements of the

932   orientations of glaucophane and tourmaline long axes were conducted on a

933   plane perpendicular to the foliation using an optical microscope. The histograms

934   are constructed to align the mean orientation (lineation) to 90°. N: total number

935   of measured grains. Note that N exceeds 15,000 in (c). Von Mises distributions

936   (as determined in the original studies) are represented by solid lines and appear

937   to fit the measured data. κ: concentration parameter for each distribution. The

938   four histograms are arranged in order of increasing κ. As the measurements

939   were made on a surface parallel to the foliation, the κ values for these data

940   satisfy $\kappa = \psi\kappa_n^+$ (Table 1). As ψ is not well constrained for these samples, we

941   were unable to evaluate κ_n^+.

942

943   Fig. 8. Selected examples of lower-hemisphere fabric diagrams (Schmidt net) for

944   columnar minerals from the literature (a and c) and corresponding contour

945   patterns for nucleation rate predicted by our model (b and d). (a) Hornblende c-

946 axes in anorthosite from Ontario, Canada; after Rousell (1981, fig. 4d). The

947 orientations of 100 grains were measured using a universal stage on an optical

948 microscope. Contours are drawn according to Kamb's (1959) statistical method.

949 F and L indicate the foliation surface and lineation, respectively. (b) Contour

950 diagram predicted by the model for $\psi = 0.21$ and $\kappa_n^+ = 2.3$.. (c) Glaucophane

951 c-axes in an eclogite (RK49) from the Tauern Window, Austria; modified after

952 Keppler et al., (2015, fig. 6). Orientations were measured using a neutron time-

953 of-flight texture diffractometer SKAT at the Frank Laboratory of Neutron Physics

954 at JINR (Dubna, Russia). Contour levels represent multiples of a uniform

955 distribution. The lineation (L) is oriented E–W and the pole to the foliation is

956 oriented N–S. (d) Contour diagram predicted by the model for $\psi = 0.002$ and

957 $\kappa_n^+ = 1.2$. For coloured contour diagrams of (b) and (d), see Fig. 4.

958

959 Fig. 9. Selected examples of 2D preferred orientations of platy minerals. N: number

960 of measured grains. (a) Two histograms showing the orientations of (001)

961 planes of individual mica grains in slate from the Nackara Arc, South Australia,

962 relative to slaty cleavage (S_1) and bedding (S_0) (modified after Bell, 1978, fig.

963 22). P8 (a1) and 012 (a2) are sample numbers. Orientations were measured on

964 a flat microscope stage on a section oriented normal to the bedding–cleavage

965 intersection lineation. We fitted the data to von Mises distributions (solid curves)

966 for grains oriented within <35° of S1 (foliation). The fit appears reasonable at

967 values of $\kappa = -2.1$ (a1) and $\kappa = -2.2$ (a2). We cannot evaluate κ_n^- due to a

968 lack of information regarding the lineation in this sample. (b) (001) histograms

969 for old (b1) and new (b2) biotite grains in a slate sample (specimen 476–67)

970 from the Fleurieu Peninsula, South Australia (modified after Mancktelow, 1979,

971 fig. 7). Orientations were measured on a section perpendicular to the foliation

972 and parallel to the lineation, using an optical microscope. Thus, the calculated

973 concentration parameter (κ) is equivalent to κ_n^- (Table 1). The histogram for the

974 new grains (b2) can be fitted to a von Mises distribution (solid curve) with a κ

975 value of –57. This κ value is equivalent to κ_0^- (Table 1). Orientation data for

976 the old grains (b1) cannot be fitted to a von Mises distribution.

977

978 Fig. 10. Examples of fabric diagrams (lower-hemisphere Schmidt nets) for platy

979 minerals (a, c, e and g) and corresponding predicted nucleation rate patterns (b,

980 d, f and h). (a) Orientations of (001) of chlorite in an argillaceous rock (Loc. 6)

981 from South Kitakami, northeast Japan (Ishii, 1988, fig. 8). Orientations were

982 measured in transmission mode with a diffractometer fitted to a universal

983 sample holder and pinhole slit. Contours represent the ratio of the distribution

984 density relative to the mean density. The distribution peak is not located at the

985 centre of the diagram. Triangle indicates the pole to bedding. (b) Predicted

986 contour pattern at $\psi = 0.9$ and $\kappa_n^- = -0.55$ (centre = σ_1). (c) Orientations of

987 (001) of mica in slate (HL–23) from Lehigh Gap, Pennsylvania, USA (Holeywell

988 and Tullis, 1975, fig. 10). Orientations were measured using an X-ray pole-

989 figure goniometer. Contours are labelled in multiples of uniform distribution. N,

990 W and D correspond to the orientation of geographical north, west and down,

991 respectively. (d) Predicted contour pattern at $\psi = 0.8$ and $\kappa_n^- = -2.5$ (centre =

992 σ_2). (e) Orientations of basal planes (00ℓ) of muscovite in slate (W22) from North

993 Wales, United Kingdom (Oertel and Phakey, 1972, fig. 2). Orientations were

994 measured using an X-ray pole-figure goniometer. Contours represent multiples

995 of random intensity (2, 4, 6, 8,10, 12, 14 and 16). N and W indicate north and

996 west, respectively. na: nadir. Dashed line: trace of bedding plane. F: fold axis

997 defined by the intersection between bedding and slaty cleavage. (f) Predicted

998 contour pattern at $\psi = 0.5$ and $\kappa_n^- = -4$ (centre = σ_1). (g) Orientations of

999 (001) of muscovite in slate from the La Fortelle quarry in the Belgian Ardennes

1000 (Wenk et al., 2018, fig. 5). Quantitative orientation analysis was conducted

1001 following the Rietveld method on a synchrotron X-ray diffraction image. Contour

1002 levels are illustrated in the legend and correspond to pole densities in multiples

1003   of a random distribution. (h) Predicted contour pattern at $\psi = 0$ and $\kappa_n^- = -14$

1004   (centre = σ_1). For coloured contour diagrams for (b), (d), (f) and (h), see Fig. 4.

1005

1006   Fig. 11. Schematic cross-section of a growing embryo on a substrate grain. (a) Step

1007   1: formation of unit cells on the substrate grain. (b) Step 2: formation of a single-

1008   layer embryo combining the unit cells. (c) Step 3: construction of a multi-layer

1009   embryo. The matrix (dotted area) in (a)–(c) is filled with stress-transmittable

1010   material. Unit cells (light grey) are unstable. See text for detail.

1011

1012

1013   Table 1. Distribution functions with respect to direction cosines (ϕ_1 and ϕ_3) on three

1014   orthogonal sections for columnar and platy minerals.

Fig. 1

Fig. 2

Fig. 3

$$f(\theta) = \frac{\exp\left[\kappa\cos 2(\theta - \pi/2)\right]}{\int_0^\pi \exp(\kappa\cos 2\theta)d\theta}$$
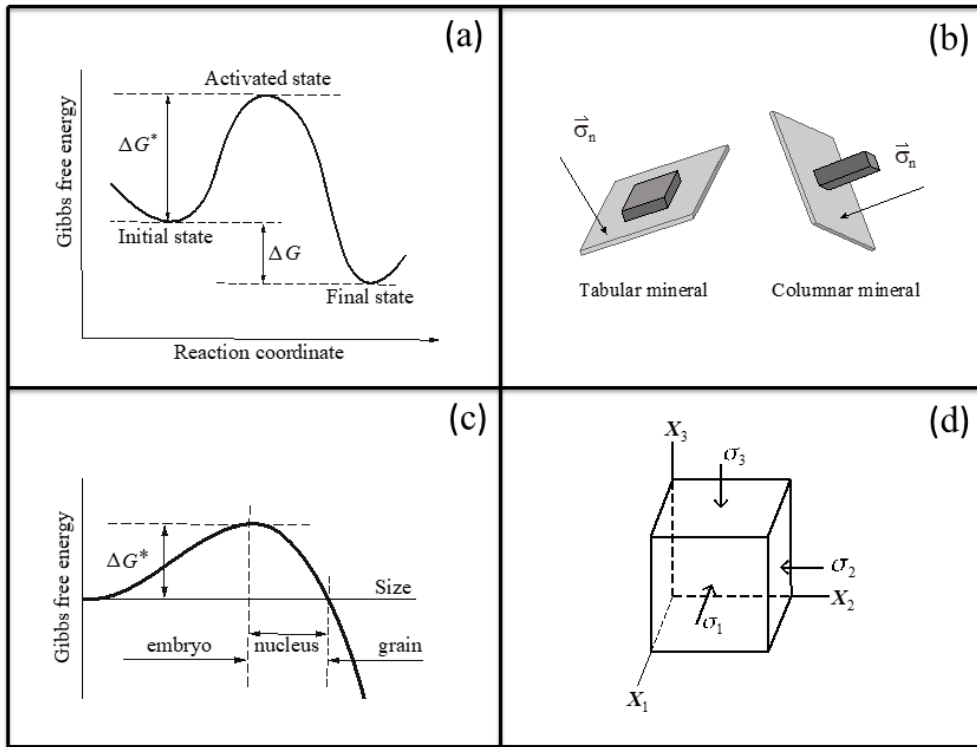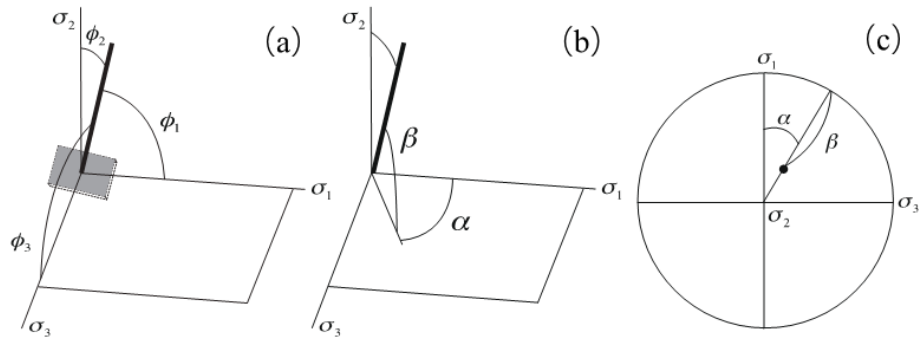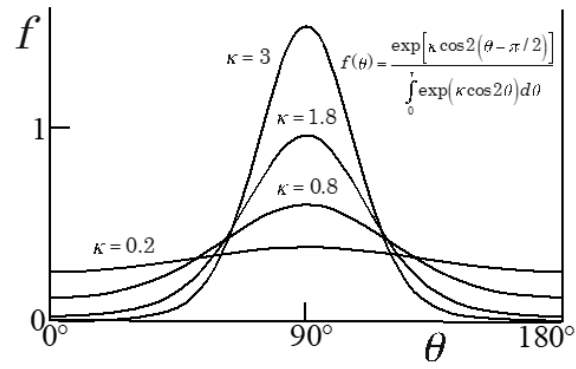
Fig.4
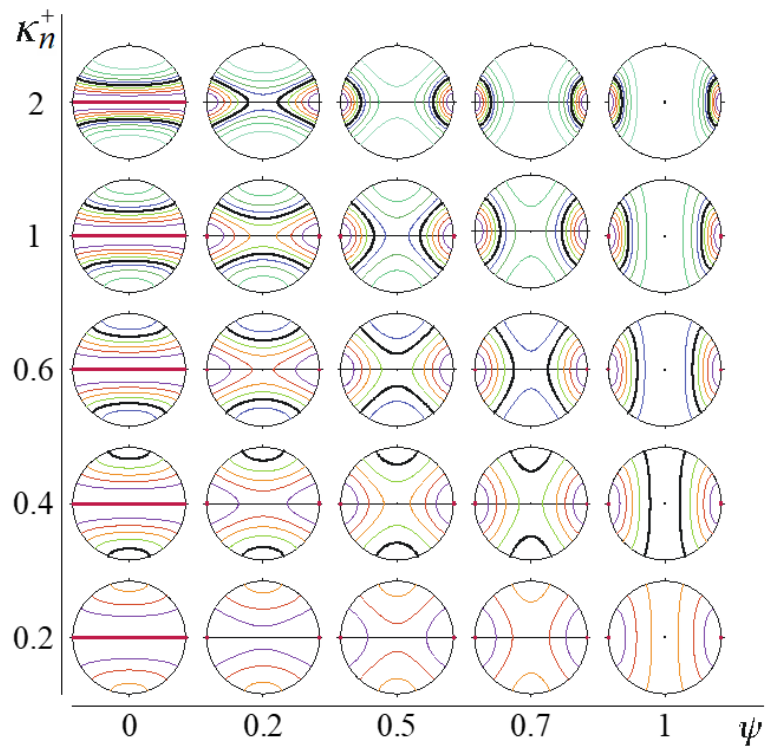
Fig. 5
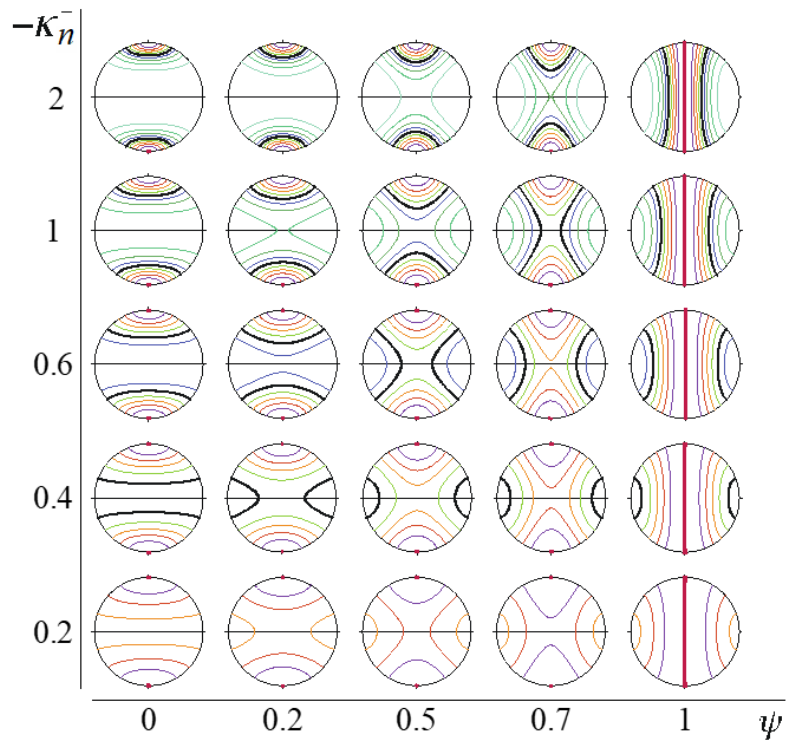
Fig. 6
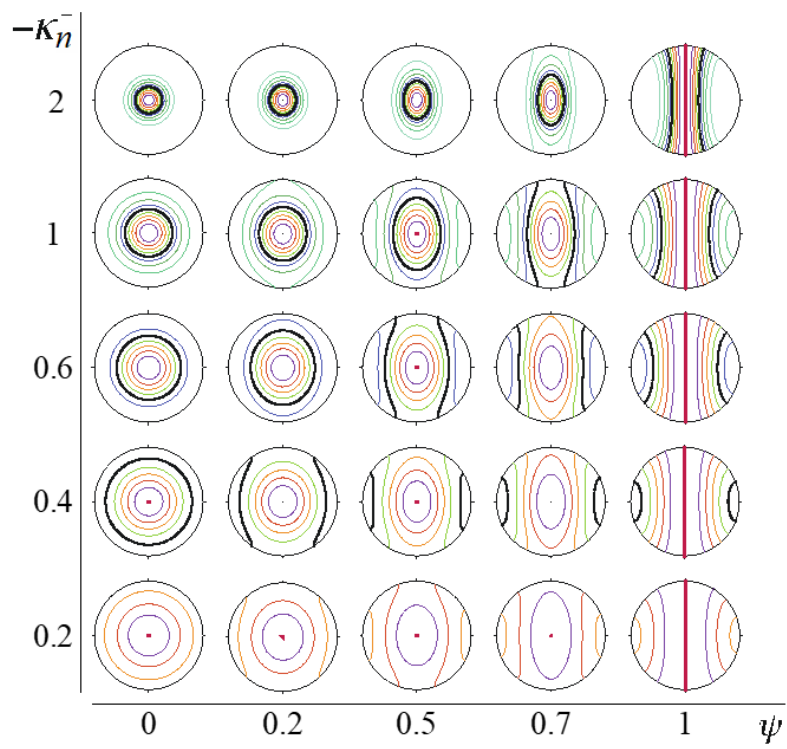
Fig. 7
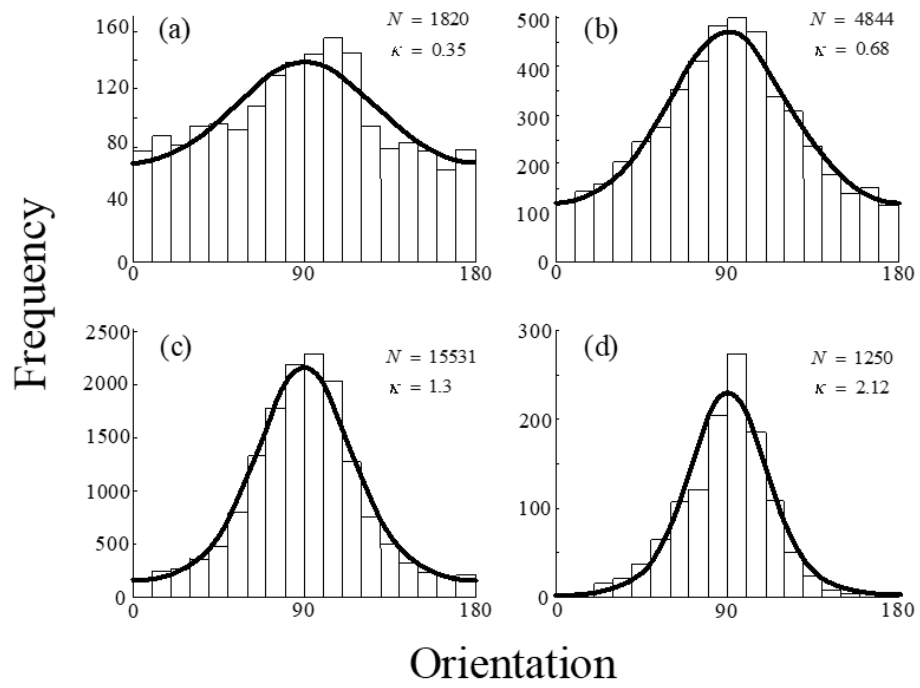
Fig. 8
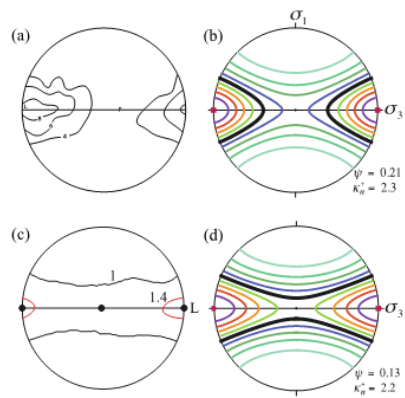
Fig. 9
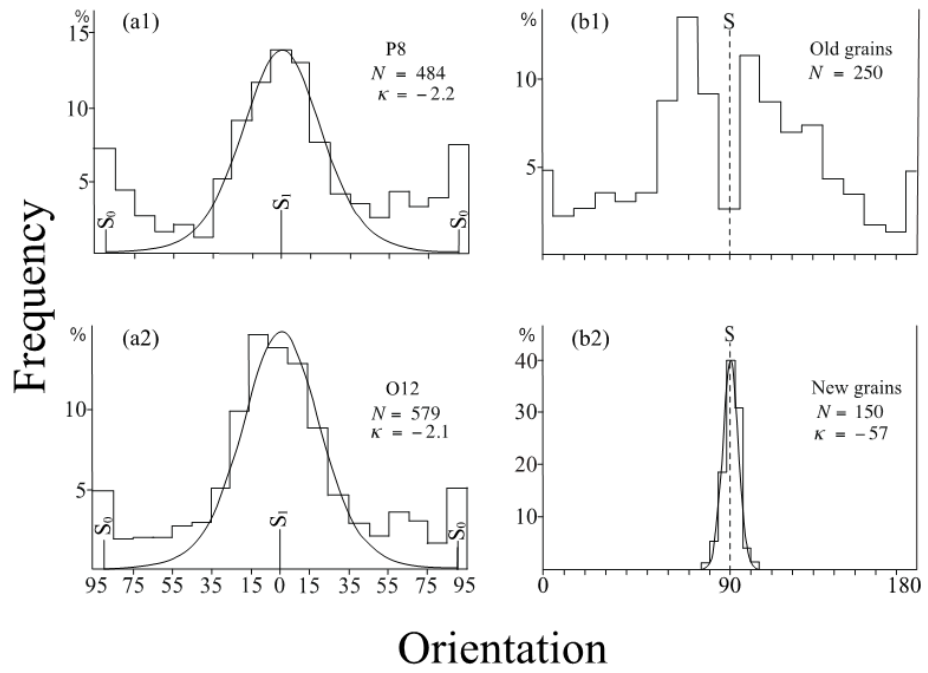
Fig. 10
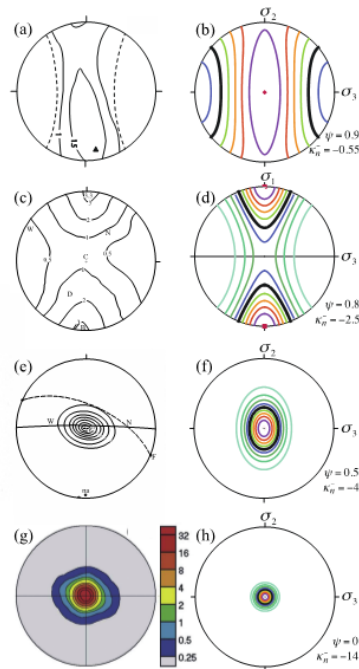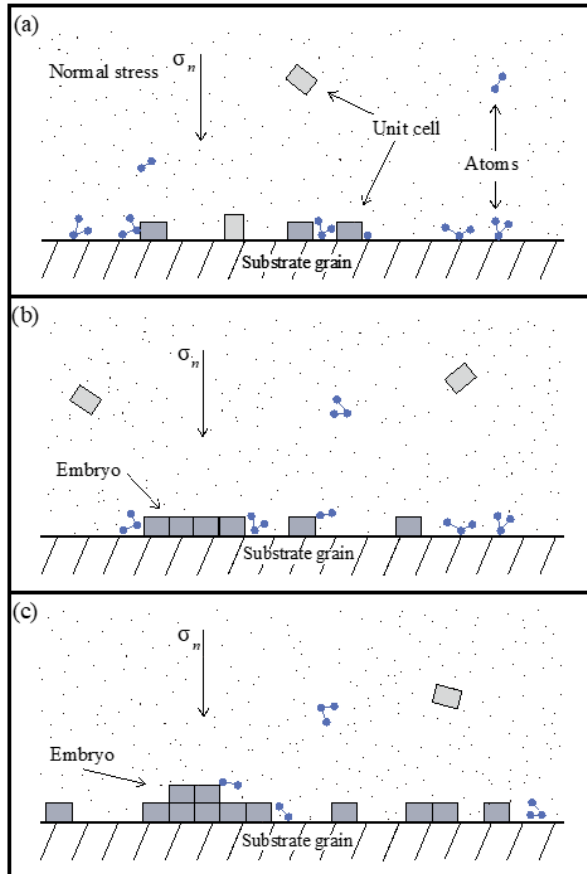
Fig. 11

Table 1

Section	Columnar minerals	Platy minerals
$x_1 - x_2$	$I(\phi_1) = A_3 \exp\left[(1 - \psi) \cdot \kappa_n^+ \cos 2\left(\phi_1 + \frac{\pi}{2}\right)\right]$	$I(\phi_1) = A_3 \exp[(\psi - 1) \cdot \kappa_n^- \cos 2\,\phi_1]$
$x_2 - x_3$	$I(\phi_3) = A_1 \exp(\psi \cdot \kappa_n^+ \cos 2\,\phi_3)$	$I(\phi_3) = A_1 \exp\left[-\psi \cdot \kappa_n^- \cos 2\left(\phi_3 + \frac{\pi}{2}\right)\right]$
$x_3 - x_1$	$I(\phi_1) = A_{13} \exp\left[\kappa_n^+ \cos 2\left(\phi_1 + \frac{\pi}{2}\right)\right]$	$I(\phi_1) = A_{13} \exp(-\kappa_n^- \cos 2\,\phi_1)$

Appendix 1. Gibbs free energy of activation during nucleation

We consider two energy parameters during nucleation under given pressure–temperature conditions: the Gibbs free energy of reaction ΔG_R and the interface energy per unit area γ (e.g., Kretz, 1994; Lasaga, 1998), which are proportional to the volume and surface area of the embryo, nucleus, or grain, respectively. For simplicity, we assume that the embryo/nucleus/grain is surrounded by a homogenous matrix.

A1.1. Spherical embryo

We first consider the case of a spherical embryo/nucleus/grain with radius r and express the overall change in Gibbs free energy ΔG as

$$\Delta G(r) = 4\pi\gamma r^2 + \frac{4}{3}\pi \cdot \Delta G_R \cdot r^3 . \qquad (A1)$$

As we consider a thermodynamically stable new phase at a given pressure and temperature, the Gibbs free energy of reaction (ΔG_R) is negative. In contrast, as the formation of a new phase generates new surfaces around the embryo/nucleus/grain, the interface energy is positive. Thus, a critical Gibbs free energy of reaction ΔG^* exists and is shown graphically in Fig. 1c.

Spherical embryos may be used to model and understand phase transformations (e.g., Kretz, 1994; Hobbs and Ord, 2015), such as the nucleation of liquid drops in gases (e.g., Smoluchowski, 1951), as well as the nucleation of crystals in magma (e.g., Vernon, 2004). The use of spherical embryos allows for a simple calculation of chemical free energy and interface energy, as only a single size parameter (the radius of the nucleus) must be considered. However, the concept of spherical embryos is clearly inconsistent with models of heterogeneous nucleation in solids, and the development of a spherical embryo on a flat substrate grain is unrealistic.
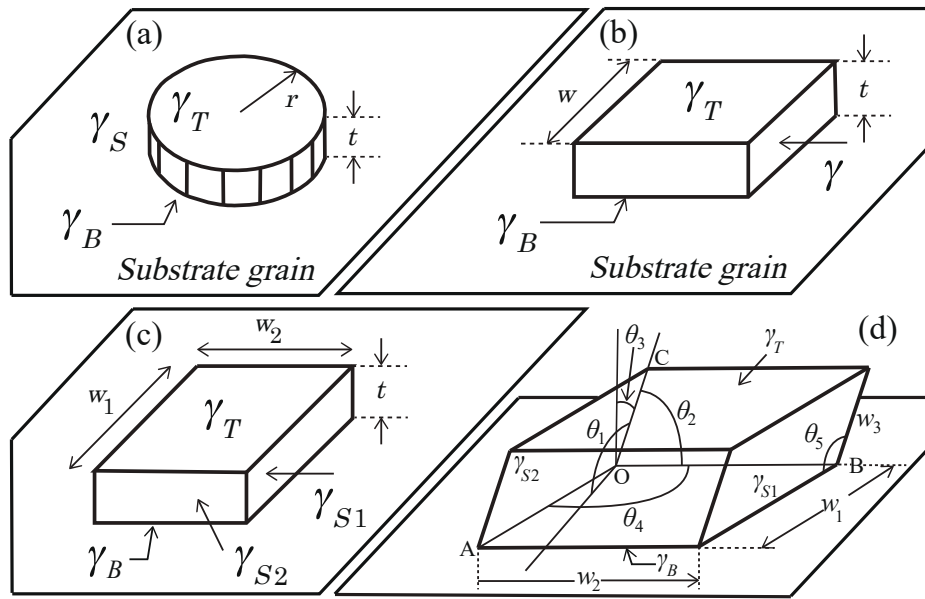
Fig. A1. Schematic diagram of an embryo on a substrate grain, showing the symbols used in the analysis. (a) Pancake-shaped embryo. r and t are the radius and thickness of the embryo, respectively. γ_B: interface energy between the new phase and the substrate grain. γ_T: interface energy between the top surface of the new phase and the matrix. γ_S: interface energy between the sides of the new phase and the matrix. (b) Cuboid embryo with a square base of width w. Thickness and interface energies are defined as in (a). (c) Cuboid embryo with a rectangular base. The two distinct widths (w_1 and w_2) of the rectangle necessitate two interface energies along the sides of the embryo (γ_{S1} and γ_{S2}). See (a) for the definition of other symbols. (d) Parallelepiped embryo on a substrate grain. w_1, w_2 and w_3 are the lengths of the three edges OA, OB and OC, respectively. Five angles ($\theta_1 - \theta_5$) are illustrated in the figure. Four interface energies are defined for the edges of the embryo, following the method in (c). Note that this diagram is only applicable to tabular minerals.

A1.2. Pancake-shaped embryo

Following Lasaga (1998, p. 547), we consider the formation of a pancake-shaped embryo on a substrate grain (Fig. A1). Three distinct interface energies are defined as follows: that between the base of the embryo and the substrate grain (γ_B), between the top surface of the embryo and the matrix (γ_T), and between the side of the embryo and the matrix (γ_S) (Fig. A1). The matrix is again assumed to be a stress-transmittable, uniform mixture of minerals and atoms (in contrast to the model of Lasaga, 1998). The thickness and radius of the embryo are designated as t and r, respectively. The overall change in ΔG becomes

$$\Delta G\left(r, t\right) = \pi r^2 \left(\gamma_B + \gamma_T\right) + 2\pi r t \gamma_S + \pi r^2 t \cdot \Delta G_R. \qquad \text{(A2)}$$

In our analysis, newly formed phases are thermodynamically stable; therefore, ΔG_R is always <0. To simplify the calculation, we define

$$\alpha = -\Delta G_R \qquad \left(\alpha > 0\right) \qquad \text{(A3)}$$

and

$$\gamma_0 = \gamma_B + \gamma_T. \qquad \text{(A4)}$$

ΔG can then be expressed as

$$\Delta G\left(r, t\right) = \pi r^2 \left(\gamma_0 - \alpha t\right) + 2\pi r t \gamma_S. \qquad \text{(A5)}$$

ΔG is influenced by the sign of the expression $\gamma_0 - \alpha t$. If $\gamma_0 - \alpha t = 0$, ΔG is ascribed to a linear function with respect to r. In this case, ΔG is always >0 and the new phase is unstable. If $\gamma_0 - \alpha t > 0$, ΔG is a quadratic function with respect to r and is always positive for any values of r and t. Thus, nucleation of a new phase is unlikely to occur.

However, nucleation will occur if $\gamma_0 - \alpha t < 0$, as a larger r results in a ΔG value of <0. As nucleation is promoted by low interface energy, we wish to determine the values of w and t that minimise the interface energy of the embryo at a given volume. We solve this problem by using Lagrange's method of undermined multipliers (e.g., Terasawa, 1960). The interface energy is defined as $2\pi\gamma_S rt + \pi\gamma_0 r^2$, with the boundary condition of $\pi r^2 t = V$, where V is the volume of the embryo. We define a new Lagrange's function as

$$L = 2\pi\gamma_S rt + \pi\gamma_0 r^2 - \lambda\left(V - \pi r^2 t\right), \qquad \text{(A6)}$$

where λ is a Lagrange's undermined multiplier. We then define the following simultaneous equations:

$$\frac{\partial L}{\partial r} = 2\pi\gamma_S t + 2\pi\gamma_0 r + 2\lambda\pi rt = 0, \qquad \text{(A7a)}$$

$$\frac{\partial L}{\partial t} = 2\pi\gamma_S r + \lambda\pi r^2 = 0. \qquad \text{(A7b)}$$

By solving these equations, we derive

$$\frac{t}{r} = \frac{\gamma_0}{\gamma_S}. \qquad \text{(A8)}$$

4

Therefore, nucleation is most likely to occur when $t/r = \gamma_0/\gamma_S$. Substituting this relation into Eq. (A2), we have

$$\Delta G(r) = -\pi\alpha \frac{\gamma_0}{\gamma_S} r^3 + 3\pi\gamma_0 r^2. \qquad \text{(A9)}$$

This is a cubic function with respect to r, and a diagram similar to that in Fig. 1c can be constructed.

A1.3. Cuboid embryo with a square base

In our model, we use a cuboid embryo with a square base (Fig. A1b), as embryos are unlikely to be pancake shaped. We again define three interface energies: between the embryo and the substrate grain, between the top of the embryos and the matrix, and between the sides of the embryo and the matrix (indicated by γ_B, γ_T and γ_S, respectively; Fig. A1). The width and thickness of the embryo are designated as w and t, respectively.

In this case, we can express ΔG as

$$\Delta G(w,t) = w^2\left(\gamma_B + \gamma_T\right) + 4wt\gamma_S + w^2 t \cdot \Delta G_R. \qquad \text{(A10)}$$

Thus, substituting $\gamma_0 = \gamma_B + \gamma_T$ and $\alpha = -\Delta G_R$, we have

$$\Delta G(w,t) = w^2\left(\gamma_0 - \alpha t\right) + 4wt\gamma_S. \qquad \text{(A11)}$$

The form of this equation is very similar to that for the pancake-shaped embryo and again states that nucleation requires the value of $\gamma_0 - \alpha t$ to be negative.

We determine w and t to minimise the interface energy of the embryo with the Lagrange's method of undetermined multipliers to solve this problem. The

interface energy is defined as $\gamma_0 w^2 + 4\gamma_S tw$ with a boundary condition of $tw^2 = V_{em}$,

where V_{em} is the volume of the embryo. We define a new Lagrange's function as

$$L = \gamma_0 w^2 + 4\gamma_S tw - \lambda(V_{em} - tw^2), \qquad \text{(A12)}$$

where λ is a Lagrange's undetermined multiplier. We then define the following simultaneous equations:

$$\frac{\partial L}{\partial w} = 2\gamma_0 w + 4\gamma_S t + 2\lambda tw = 0 \qquad \text{(A13)}$$

and

$$\frac{\partial L}{\partial t} = 4\gamma_S w + \lambda w^2 = 0. \qquad \text{(A14)}$$

By solving these equations, we attain a relation for the minimum interface energy:

$$\frac{w}{t} = \frac{2\gamma_S}{\gamma_0}. \qquad \text{(A15)}$$

If a new phase satisfies the relation $\gamma_0 = 2\gamma_S$, it is likely to have a cubic shape ($w = t$). From empirical observations of typical mineral grains, we define platy and columnar minerals as having w/t ratios that satisfy $\gamma_0 < 2\gamma_S$ and $\gamma_0 > 2\gamma_S$, respectively (Fig. A1).

We can then calculate ΔG for a rectangular embryo:

$$\Delta G(w, t) = \gamma_0 w^2 + 4\gamma_S tw + tw^2 \cdot \Delta G_R. \qquad \text{(A16)}$$

Note that $\Delta G_R < 0$. Substituting the ideal w/t relation of Eq. (A15) into Eq. (A10), we have

$$\Delta G(t) = \frac{4\gamma_S^2 \cdot \Delta G_R}{\gamma_0^2} t^3 + \frac{12\gamma_S^2}{\gamma_0} t^2. \qquad \text{(A17)}$$

ΔG is a cubic function with respect to t, which first increases, attains a maximum, and then rapidly decreases with increasing t (Fig. 1c).

A1.4. Cuboid embryo with a rectangular base

To generalise our model to all cuboid embryos, we now consider the case of a cuboid embryo with a rectangular base (Fig. A1). Four different interface energies are discriminated: between substrate grains (γ_B), between the top of the substrate grain and the matrix (γ_T), and between the two sides of the substrate grain and the matrix (γ_{S1} and γ_{S2}) (Fig. A1). Each pair of opposing interface energies are set equivalents. The matrix is assumed to be a uniform mixture of various minerals and atoms. The two widths and the thickness of the embryo are represented by w_1, w_2 and t, respectively.

In this scenario, ΔG can be expressed as

$$\Delta G\left(w_1, w_2, t\right) = w_1 w_2 \left(\gamma_B + \gamma_T\right) + 2t\left(w_1 \gamma_{S1} + w_2 \gamma_{S2}\right) + t w_1 w_2 \cdot \Delta G_R$$

$$= w_1 w_2 \left(\gamma_0 - \alpha t\right) + 2t\left(w_1 \gamma_{S1} + w_2 \gamma_{S2}\right), \qquad \text{(A18)}$$

7

where $\gamma_0 = \gamma_B + \gamma_T$ and $\alpha = -\Delta G_R$. In this case, the relation $\gamma_0 - \alpha t < 0$ must be satisfied for nucleation to occur. Thus, a nucleus or grain with a unit-cell thickness cannot form. Thickening of the embryo is necessary for nucleation to occur.

We obtain w_1, w_2 and t to minimise the total interface energy of the embryo with the Lagrange's method of undetermined multipliers to solve this problem. The total interface energy is defined as $\gamma_0 w_1 w_2 + 2t(\gamma_{S1} w_1 + \gamma_{S2} w_2)$, with a constant boundary condition of $t w_1 w_2 = V_{em}$. We define a new Lagrange's function as

$$L = \gamma_0 w_1 w_2 + 2t\left(\gamma_{S1} w_1 + \gamma_{S2} w_2\right) - \lambda\left(V_{em} - t w_1 w_2\right), \qquad \text{(A19)}$$

where λ is a Lagrange's undetermined multiplier. We then derive the following simultaneous equations:

$$\frac{\partial L}{\partial w_1} = \gamma_0 w_2 + 2\gamma_{S1} t + \lambda t w_2 = 0, \qquad \text{(A20a)}$$

$$\frac{\partial L}{\partial w_2} = \gamma_0 w_1 + 2\gamma_{S2} t + \lambda t w_1 = 0, \qquad \text{(A20b)}$$

$$\frac{\partial L}{\partial t} = 2\left(w_1 \gamma_{S1} + w_2 \gamma_{S2}\right) + \lambda w_1 w_2 = 0. \qquad \text{(A20c)}$$

By solving these equations, we obtain

$$w_1 = \frac{2\gamma_{S2}}{\gamma_0} t, \qquad \text{(A21a)}$$

$$w_2 = \frac{2\gamma_{S1}}{\gamma_0} t. \qquad \text{(A21b)}$$

These equations are independent of $\alpha(-\Delta G_R)$. Substituting the ideal relations between w_1 and t (Eq. A21a) and between w_2 and t (Eq. A21b) into Eq. (A18), we derive

$$\Delta G(t) = \frac{4\gamma_{S1}\gamma_{S2}\Delta G_R}{\gamma_0^2}t^3 + \frac{12\gamma_{S1}\gamma_{S2}}{\gamma_0}t^2 . \qquad \text{(A22)}$$

This expression is a cubic function with respect to the thickness of the nuclei, and its appearance is similar to that in Fig. 2.

A1.5. Parallelepiped embryo

In a similar manner, we consider a parallelepiped embryo, which comprises three pairs of parallelograms (Fig. A1d). Note that this case is only applicable to tabular minerals. The lengths of the three edges are represented by $w_1 - w_3$ and the five angles between the edges are represented by $\theta_1 - \theta_5$. Lengths will vary during nucleation, whereas the angles are constants that are controlled by the crystallography of the nucleating mineral. The interface energies for each side are represented by γ_B, γ_T, γ_{S1} and γ_{S2}. We can express ΔG as

$$\Delta G\left(w_1, w_2, w_3\right) = \left(\gamma_B + \gamma_T\right)w_1 w_2 \sin\theta_4 + 2\gamma_{S2}w_2 w_3 \sin\theta_2 + 2\gamma_{S1}w_1 w_3 \sin\theta_5$$
$$+ \Delta G_R w_1 w_2 w_3 \cos\theta_3 \sin\theta_4 . \qquad \text{(A23)}$$

To minimise the interface energy at a given volume, we use Lagrange's method of the undetermined multiplier and define a Lagrange's function L as follows:

$$L = \gamma_0 w_1 w_2 \sin\theta_4 + 2\gamma_{S2}w_2 w_3 \sin\theta_2 + 2\gamma_{S1}w_1 w_3 \sin\theta_5 - \lambda\left(V_{em} - w_1 w_2 w_3 \cos\theta_3 \sin\theta_4\right),$$

(A24)

9

where $\gamma_0 = \gamma_B + \gamma_T$ and V_{em} is the volume of the embryo. We then derive the following simultaneous equations:

$$\frac{\partial L}{\partial w_1} = \gamma_0 w_2 \sin\theta_4 + 2\gamma_{S1} w_3 \sin\theta_5 + \lambda w_2 w_3 \cos\theta_3 \sin\theta_4 = 0, \qquad \text{(A25a)}$$

$$\frac{\partial L}{\partial w_2} = \gamma_0 w_1 \sin\theta_4 + 2\gamma_{S2} w_3 \sin\theta_2 + \lambda w_1 w_3 \cos\theta_3 \sin\theta_4 = 0, \qquad \text{(A25b)}$$

$$\frac{\partial L}{\partial w_3} = 2\gamma_{S2} w_2 \sin\theta_2 + 2\gamma_{S1} w_1 \sin\theta_5 + \lambda w_1 w_2 \cos\theta_3 \sin\theta_4 = 0. \qquad \text{(A25c)}$$

By solving these equations, we obtain

$$w_1 = \frac{2\gamma_{S2} \sin\theta_2}{\gamma_0 \sin\theta_4} w_3, \qquad \text{(A26a)}$$

$$w_2 = \frac{2\gamma_{S1} \sin\theta_5}{\gamma_0 \sin\theta_4} w_3. \qquad \text{(A26b)}$$

Substituting these ideal values into Eq. (A26a and b) and Eq. (A23), we derive

$$\Delta G(w_3) = C_1 w_3^3 + C_2 w_3^2, \qquad \text{(A27)}$$

where

$$C_1 = \frac{4\gamma_{S1}\gamma_{S2} \sin\theta_2 \cos\theta_3 \sin\theta_5 \cdot \Delta G_R}{\gamma_0^2 \sin\theta_4}, \qquad \text{(A28a)}$$

$$C_2 = \frac{4\left(\gamma_B + \gamma_T\right)\gamma_{S1}\gamma_{S2} \sin\theta_2 \sin\theta_5}{\gamma_0^2 \sin\theta_4} + \frac{8\gamma_{S1}\gamma_{S2} \sin\theta_2 \sin\theta_5}{\gamma_0 \sin\theta_4}. \qquad \text{(A28b)}$$

10

Thus, ΔG is a cubic function with respect to w_3 and its appearance is similar to that shown in Fig. 1c.

Appendix 2. The von Mises distribution

Circular data are well represented by the probability density function known as the von Mises distribution (e.g., von Mises, 1918; Mardia, 1972; Batchelet, 1981: Fisher, 1993), which is defined as

$$f(\theta) = \frac{1}{\pi I_0(\kappa)} \exp\left[\kappa \cos 2(\theta - \bar{\theta})\right], \qquad (A29)$$

where κ is the concentration parameter ($\kappa \geq 0$), θ is the angle from the mean orientation ($\bar{\theta}$), and $I_0(\kappa)$ is a modified Bessel function of the first kind. Therefore, we can derive:

$$I_0(\kappa) = \sum_{r=0}^{\infty} \frac{1}{r!^2(r+1)} \left(\frac{\kappa}{2}\right)^{1+2r}, \qquad (A30)$$

where r is a dummy integer between 0 and ∞. We chose $\bar{\theta} = 0$ when measuring the angle θ from the mean orientation $\bar{\theta}$. This simplifies the probability density function (Eq. (A29)) to

$$f(\theta) = \frac{1}{\pi I_0(\kappa)} \exp\left[\kappa \cos 2\theta\right]. \qquad (A31)$$

The pre-exponential term ($1/\pi I_0(\kappa)$) is added attached to satisfy

$$1 = \int_0^{\pi} f(\theta) \, d\theta. \qquad (A32)$$

As κ should be positive in Eq. (A31), a modification is required to account for a negative pre-cosine constant. Given that

$$\cos 2\left(\theta + \frac{\pi}{2}\right) = -\cos 2\theta, \qquad \text{(A33)}$$

we can derive, for example,

$$\exp\left(\kappa_n^- \cos 2\theta\right) = \exp\left[-\kappa_n^- \cos 2\left(\theta + \frac{\pi}{2}\right)\right], \qquad \text{(A34)}$$

which produces a positive $-\kappa_0^-$ value. Therefore, we use a similar conversion from θ to $\theta + \pi/2$ when the pre-cosine constant is negative.

Appendix 3. Derivation of nucleation-rate equations

As the derivation of Eqs. (27)–(29) from Eq. (13) is not straightforward, we describe it here in detail.

A3.1. $x_1 - x_2$ plane

Substituting $n = 0$, $l = \cos\varphi_1$, $m = \sin\varphi_1$, $\sigma_2 = \psi\sigma_1 + (1 - \psi)\sigma_3$ and

$\sigma_1 - \sigma_3 = \Delta\sigma$ into Eq. (13), we obtain

$$I(l, m, 0) = A_0 \exp\left[-\frac{(\sigma_1 l^2 + \sigma_2 m^2)\Delta V^*}{k_B T}\right]$$

$$= A_0 \exp\left\{-\frac{\left[\sigma_1 l^2 + \left(\psi\sigma_1 + (1-\psi)\sigma_3\right)m^2\right]\Delta V^*}{k_B T}\right\}$$

$$= A_0 \exp\left\{-\frac{\left[\sigma_1 l^2 + \left(\psi\sigma_1 + \sigma_3 - \psi\sigma_3\right)m^2\right]\Delta V^*}{k_B T}\right\}$$

$$= A_0 \exp\left\{-\frac{\left[\sigma_1 \cos^2\varphi_1 + \left(\psi\sigma_1 + \sigma_3 - \psi\sigma_3\right)\sin^2\varphi_1\right]\Delta V^*}{k_B T}\right\}$$

$$= A_0 \exp\left\{-\frac{\left[\frac{1}{2}\left(\sigma_1 + \psi\sigma_1 + \sigma_3 - \psi\sigma_3\right) + \frac{1}{2}\left(\sigma_1 - \psi\sigma_1 - \sigma_3 + \psi\sigma_3\right)\cos 2\varphi_1\right]\Delta V^*}{k_B T}\right\}$$

$$= A_0 \exp\left[-\frac{\left(\sigma_1 + \psi\sigma_1 + \sigma_3 - \psi\sigma_3\right)\Delta V^*}{2k_B T}\right]\exp\left[-\frac{\left(\sigma_1 - \psi\sigma_1 - \sigma_3 + \psi\sigma_3\right)\cos 2\varphi_1 \Delta V^*}{2k_B T}\right]$$

$$= A_0 \exp\left[-\frac{\left(\sigma_1 + \psi\sigma_1 + \sigma_3 - \psi\sigma_3\right)\Delta V^*}{2k_B T}\right]\exp\left[-\frac{\left(1-\psi\right)\left(\sigma_1 - \sigma_3\right)\cos 2\varphi_1 \Delta V^*}{2k_B T}\right]$$

$$= A_{13} \exp\left[-\frac{(1-\psi)\Delta\sigma \cdot \Delta V^*}{2k_B T} \cos 2\varphi_1 \right]$$

$$= A_3 \exp\left[(\psi-1)\kappa_n^{\pm} \cos 2\varphi_1 \right], \qquad\qquad (A35)$$

where

$$\kappa_n^{\pm} = \frac{\Delta\sigma \cdot \Delta V^*}{2k_B T} \qquad\qquad (A36)$$

and

$$A_3 = A_0 \exp\left[-\frac{(\sigma_1 + \psi\sigma_1 + \sigma_3 - \psi\sigma_3)\Delta V^*}{2k_B T} \right]. \qquad (A37)$$

Thus, to assign positive pre-cosine factors, Eq. (A35) is written separately for columnar and platy minerals by using κ_n^+ and κ_n^- (Eq. (21)) as follows:

$$I(\varphi_1) = A_3 \exp\left| (1-\psi)\kappa_n^+ \cos 2\left(\varphi_1 + \frac{\pi}{2} \right) \right| \qquad \text{(columnar minerals)} \quad (A38a)$$

$$I(\varphi_1) = A_3 \exp\left[(\psi-1)\kappa_n^- \cos 2\varphi_1 \right]. \qquad \text{(platy minerals)} \qquad (A38b)$$

A3.2. $x_2 - x_3$ plane

Substituting $l=0$, $n=\cos\varphi_3$, $m=\sin\varphi_3$, $\sigma_2 = \psi\sigma_1 + (1-\psi)\sigma_3$ and

$\sigma_1 - \sigma_3 = \Delta\sigma$ into Eq. (13), we obtain

$$I(0,\ m,\ n) = A_0 \exp\left[-\frac{(\sigma_2 m^2 + \sigma_3 n^2)\Delta V^*}{k_B T}\right]$$

$$= A_0 \exp\left\{-\frac{\left[\left(\psi\sigma_1 + (1-\psi)\sigma_3\right)m^2 + \sigma_3 n^2\right]\Delta V^*}{k_B T}\right\}$$

$$= A_0 \exp\left\{-\frac{\left[\left(\psi\sigma_1 + \sigma_3 - \psi\sigma_3\right)\sin^2\varphi_3 + \sigma_3\cos^2\varphi_3\right]\Delta V^*}{k_B T}\right\}$$

$$= A_0 \exp\left\{-\frac{\left[\frac{1}{2}\left(\psi\sigma_1 + 2\sigma_3 - \psi\sigma_3\right) + \frac{1}{2}\left(\psi\sigma_3 - \psi\sigma_1\right)\cos 2\varphi_3\right]\Delta V^*}{k_B T}\right\}$$

$$= A_0 \exp\left[-\frac{\left(\psi\sigma_1 + 2\sigma_3 - \psi\sigma_3\right)\Delta V^*}{2k_B T}\right]\exp\left\{\frac{\psi\left(\sigma_1 - \sigma_3\right)\cos 2\varphi_3\Delta V^*}{2k_B T}\right\}$$

$$= A_1 \exp\left\{\frac{\psi\cdot\Delta\sigma\cdot\Delta V^*}{2k_B T}\cos 2\varphi_3\right\}$$

$$= A_1 \exp\left(\psi\cdot\kappa_n^{\pm}\cos 2\varphi_3\right) \qquad\qquad \text{(A39)}$$

where

$$A_1 = A_0 \exp\left[-\frac{\left(\psi\sigma_1 + 2\sigma_3 - \psi\sigma_3\right)\Delta V^*}{2k_B T}\right]. \qquad\qquad \text{(A40)}$$

Equation (A39) is written separately for columnar and platy minerals, as follows:

$$I(\varphi_3) = A_1 \exp\left(\psi\kappa_n^{+}\cos 2\varphi_3\right), \qquad \text{(columnar minerals)} \qquad \text{(A41a)}$$

$$I(\varphi_3) = A_1 \exp\left[-\psi\kappa_n^{-}\cos 2\left(\varphi_3 + \frac{\pi}{2}\right)\right]. \qquad \text{(platy minerals)} \qquad \text{(A41b)}$$

16

A3.3. $x_3 - x_1$ *plane*

Substituting $m = 0$, $l = \cos\varphi_1$, $n = \sin\varphi_1$, $\sigma_2 = \psi\sigma_1 + (1-\psi)\sigma_3$ and

$\sigma_1 - \sigma_3 = \Delta\sigma$ into Eq. (13), we obtain

$$
\begin{aligned}
I(l, 0, n) &= A_0 \exp\left[-\frac{(\sigma_1 l^2 + \sigma_3 n^2)\Delta V^*}{k_B T}\right] \\[2em]
&= A_0 \exp\left[-\frac{(\sigma_1 \cos^2\varphi_1 + \sigma_3 \sin^2\varphi_1)\Delta V^*}{k_B T}\right] \\[2em]
&= A_0 \exp\left\{-\frac{\left[\frac{1}{2}(\sigma_1 + \sigma_3) + \frac{1}{2}(\sigma_1 - \sigma_3)\cos 2\varphi_1\right]\Delta V^*}{k_B T}\right\} \\[2em]
&= A_0 \exp\left[-\frac{(\sigma_1 + \sigma_3)\Delta V^*}{2k_B T}\right]\exp\left[-\frac{(\sigma_1 - \sigma_3)\Delta V^* \cos 2\varphi_1}{2k_B T}\right] \\[2em]
&= A_0 \exp\left[-\frac{(\sigma_1 + \sigma_3)\Delta V^*}{2k_B T}\right]\exp\left(-\frac{\Delta\sigma \cdot \Delta V^*}{2k_B T}\cos 2\varphi_1\right) \\[2em]
&= A_{13} \exp\left[\kappa_n^{\pm}\cos 2\left(\varphi_1 + \frac{\pi}{2}\right)\right], \qquad\qquad \text{(A42)}
\end{aligned}
$$

where

$$
A_{13} = A_0 \exp\left[-\frac{(\sigma_1 + \sigma_3)\Delta V^*}{2k_B T}\right]. \qquad\qquad \text{(A43)}
$$

Equation (A42) is written separately for columnar and platy minerals, as follows:

$$I(\varphi_1) = A_{13} \exp\left[\kappa_n^+ \cos 2\left(\varphi_1 + \frac{\pi}{2}\right)\right], \qquad \text{(columnar minerals)} \qquad \text{(A44a)}$$

$$I(\varphi_1) = A_{13} \exp\left(-\kappa_n^- \cos 2\varphi_1\right). \qquad \text{(platy minerals)} \qquad \text{(A44b)}$$

Appendix 4. Direction cosines and stereographic projection

Stereographic projection is performed using α and β angles (Fig. 2b and c). Thus, we require a translation between two sets of angles. Figure 2a and b presents schematic diagrams showing the same feature defined by different sets of angles. We use an upper-hemisphere stereographic projection; however, the two hemispheres of the projection are equivalent due to the symmetry of the nucleation-rate equation with respect to the three coordinate axes. As

$\beta = 90° - \varphi_1$ (Fig. 2b), we can express (l, m, n) in terms of α and β as follows:

$$l = \cos\alpha\cos\beta, \qquad \text{(A45a)}$$
$$m = \sin\beta, \qquad \text{(A45b)}$$
$$n = \sin\alpha\cos\beta. \qquad \text{(A45c)}$$

Appendix 5. Contours on stereographic projections

A5.1. Columnar minerals

We derive an equation in terms of stereographic angles (α and β) that produce identical nucleation rates for all columnar minerals. We define d ($0 < d < 1$) as

$$d = \frac{I(l, m, n)}{I(0, 0, 1)}, \qquad (A46)$$

which can be used to derive the following simple equation:

$$d = \frac{I(l, m, n)}{I(0, 0, 1)} = \frac{A_0 \exp\left[-\dfrac{(\sigma_1 l^2 + \sigma_2 m^2 + \sigma_3 n^2)\Delta V^+}{k_B T}\right]}{A_0 \exp\left(-\dfrac{\sigma_3 \Delta V^+}{k_B T}\right)}$$

$$= \exp\left[-\frac{(\sigma_1 l^2 + \sigma_2 m^2 + \sigma_3 n^2 - \sigma_3)\Delta V^+}{k_B T}\right]$$

$$= \exp\left\{\frac{\left[-\sigma_1 l^2 - \sigma_2 m^2 + (1 - n^2)\sigma_3\right]\Delta V^+}{k_B T}\right\}$$

$$= \exp\left\{\frac{\left[-\sigma_1 l^2 - \sigma_2 m^2 + (l^2 + m^2)\sigma_3\right]\Delta V^+}{k_B T}\right\}$$

$$= \exp\left\{-\frac{\left[\sigma_1 l^2 + \sigma_2 m^2 - (l^2 + m^2)\sigma_3\right]\Delta V^+}{k_B T}\right\}$$

$$= \exp\left\{-\frac{\left[(\sigma_1 - \sigma_3)l^2 + (\sigma_2 - \sigma_3)m^2\right]\Delta V^+}{k_B T}\right\}$$

$$= \exp\left\{-\frac{\left[(\sigma_1 - \sigma_3)l^2 + \psi(\sigma_1 - \sigma_3)m^2\right]\Delta V^+}{k_B T}\right\}$$

$$= \exp\left\{-\frac{\left[(\sigma_1 - \sigma_3)(l^2 + \psi m^2)\right]\Delta V^+}{k_B T}\right\}. \qquad \text{(A47)}$$

Thus, we derive

$$\frac{1}{d} = \exp\left[\frac{\left(l^2 + \psi m^2\right)\Delta\sigma \cdot \Delta V^+}{k_B T}\right], \qquad \text{(A48)}$$

and, by taking the natural logarithm of both sides, we obtain

$$\ln\left(\frac{1}{d}\right) = \frac{\left(l^2 + \psi m^2\right)\Delta\sigma \cdot \Delta V^+}{k_B T}. \qquad \text{(A49)}$$

Thus,

$$\frac{k_B T}{\Delta\sigma \cdot \Delta V^+}\ln\left(\frac{1}{d}\right) = l^2 + \psi m^2. \qquad \text{(A50)}$$

The above equation is rewritten in terms of α and β (Appendix 4 in this online supplementary material) as follows:

$$\frac{k_B T}{\Delta\sigma \cdot \Delta V^+}\ln\left(\frac{1}{d}\right) = \cos^2\alpha\cos^2\beta + \psi\sin^2\beta. \qquad \text{(A51)}$$

As $\kappa_n^+ = \Delta\sigma \cdot \Delta V^+ / 2k_B T$, we have

$$\frac{\ln(1/d)}{2\kappa_n^+} = \cos^2\alpha\cos^2\beta + \psi\sin^2\beta$$

$$= \cos^2\alpha\cos^2\beta + \psi(1 - \cos^2\beta)$$

$$= \cos^2\alpha\cos^2\beta + \psi - \psi\cos^2\beta)$$

$$= (\cos^2\alpha - \psi)\cos^2\beta + \psi. \qquad \text{(A52)}$$

Thus, we derive

$$\frac{\ln(1/d)}{2\kappa_n^+} - \psi = (\cos^2 \alpha - \psi)\cos^2 \beta. \qquad \text{(A53)}$$

From this, we have

$$\cos^2 \beta = \frac{\left[\dfrac{\ln(1/d)}{2\kappa_n^+} - \psi\right]}{\cos^2 \alpha - \psi}, \qquad \text{(A54)}$$

which allows us to derive an equation to calculate β:

$$\cos \beta = \pm\sqrt{\frac{\left[\dfrac{\ln(1/d)}{2\kappa_n^+} - \psi\right]}{\cos^2 \alpha - \psi}}. \qquad \text{(A55)}$$

A5.2. Platy minerals

We derive an equation in terms of α and β that produces identical nucleation rates for all platy minerals. We define d (0 < d < 1) to represent the proportion of the nucleation rate at (l, m, n) with respect to the maximum nucleation rate, as follows:

$$d = \frac{I(l, m, n)}{I(1, 0, 0)}, \qquad \text{(A56)}$$

which allows the derivation of the following simple equation:

$$d = \frac{I(l, m, n)}{I(1, 0, 0)} = \frac{A_0 \exp\left(-\dfrac{(\sigma_1 l^2 + \sigma_2 m^2 + \sigma_3 n^2)\Delta V^-}{k_B T}\right)}{A_0 \exp\left(-\dfrac{\sigma_1 \Delta V^-}{k_B T}\right)}$$

$$= \exp \left\{ \frac{\Delta V^-}{k_B T} \left[-\left(\sigma_1 l^2 + \sigma_2 m^2 + \sigma_3 n^2 \right) + \sigma_1 \right] \right\}. \qquad \text{(A57)}$$

Taking the natural logarithm of both sides, we have

$$\ln d = \frac{\Delta V^-}{k_B T} \left[-\left(\sigma_1 l^2 + \sigma_2 m^2 + \sigma_3 n^2 \right) + \sigma_1 \right]. \qquad \text{(A58)}$$

Thus,

$$\frac{k_B T}{\Delta V^-} \ln d = \sigma_1 - \left(\sigma_1 l^2 + \sigma_2 m^2 + \sigma_3 n^2 \right)$$

$$= \sigma_1 \left(1 - l^2 \right) - \left(\sigma_2 m^2 + \sigma_3 n^2 \right)$$

$$= \sigma_1 \left(m^2 + n^2 \right) - \left(\sigma_2 m^2 + \sigma_3 n^2 \right)$$

$$= \left(\sigma_1 - \sigma_2 \right) m^2 + \left(\sigma_1 - \sigma_3 \right) n^2$$

$$= (1 - \psi) \left(\sigma_1 - \sigma_3 \right) m^2 + \left(\sigma_1 - \sigma_3 \right) n^2. \qquad \text{(A59)}$$

Therefore, we have

$$\frac{k_B T}{(\sigma_1 - \sigma_3) \Delta V^-} \ln d = (1 - \psi) m^2 + n^2. \qquad \text{(A60)}$$

Orientations (l, m, n) can be expressed in terms of α and β as $\cos\alpha \cdot \cos\beta$, $\sin\beta$ and $\sin\alpha \cdot \cos\beta$, respectively (Eq. (A29)). Thus, by using $\Delta\sigma = \sigma_1 - \sigma_3$ we obtain

$$\frac{k_B T}{\Delta \sigma_1 \cdot \Delta V^-} \ln d = (1-\psi)\sin^2\beta + \sin^2\alpha \cdot \cos^2\beta. \qquad \text{(A61)}$$

As $\kappa_n^- = \Delta\sigma \cdot \Delta V^- / 2k_B T$, we have

$$\frac{\ln d}{2\kappa_n^-} = (1-\psi)\sin^2\beta + \sin^2\alpha \cdot \cos^2\beta$$
$$= (1-\psi)(1-\cos^2\beta) + \sin^2\alpha \cdot \cos^2\beta$$
$$= (1-\psi) - (1-\psi)\cos^2\beta + \sin^2\alpha \cdot \cos^2\beta$$
$$= (1-\psi) + (\sin^2\alpha + \psi - 1)\cos^2\beta$$
$$= (1-\psi) + (\psi - \cos^2\alpha)\cos^2\beta. \qquad \text{(A62)}$$

Finally, we derive

$$\frac{\ln d}{2\kappa_n^-} + (\psi - 1) = (\psi - \cos^2\alpha)\cos^2\beta. \qquad \text{(A63)}$$

From this, we derive

$$\cos^2\beta = \frac{\left[\dfrac{\ln d}{2\kappa_n^-} + (\psi - 1)\right]}{\psi - \cos^2\alpha}. \qquad \text{(A64)}$$

Thus, we can calculate β using

$$\cos\beta = \pm\sqrt{\frac{\left[\dfrac{\ln d}{2\kappa_n^-} + (\psi - 1)\right]}{\psi - \cos^2\alpha}}. \qquad \text{(A65)}$$

A5.3. Graphical projection of contours

Contours derived from our analysis were drawn on equal-area stereographic diagrams using the following equations, with reference to the horizontal (x) and

vertical (y) axes:

$$x = R\sqrt{2}\sin\left(\frac{\pi}{4} - \frac{\beta}{2}\right)\cdot\sin\alpha, \qquad \text{(A66a)}$$

$$y = R\sqrt{2}\sin\left(\frac{\pi}{4} - \frac{\beta}{2}\right)\cdot\cos\alpha, \qquad \text{(A66b)}$$

where R is the radius of the stereographic projection diagram (e.g., Hobbs et al., 1976, p. 499). In our analysis, we define $R = 1$.

For columnar minerals, β is given from Eq. (A55) as follows:

$$\beta = \cos^{-1}\left[\pm\sqrt{\frac{\sqrt{\dfrac{\ln(1/d)}{2\kappa_n^+}} - \psi}{\cos^2\alpha - \psi}}\right]. \qquad \text{(A67)}$$

Thus, x and y can be expressed in terms of ψ, κ_n^+ and d as

$$x = \sqrt{2}\sin\left\{\frac{\pi}{4} - \frac{1}{2}\left[\cos^{-1}\left(\pm\sqrt{\frac{\sqrt{\dfrac{\ln(1/d)}{2\kappa_n^+}} - \psi}{\cos^2\alpha - \psi}}\right)\right]\right\}\cdot\sin\alpha \qquad \text{(A68a)}$$

$$y = \sqrt{2}\sin\left\{\frac{\pi}{4} - \frac{1}{2}\left[\cos^{-1}\left(\pm\sqrt{\frac{\sqrt{\dfrac{\ln(1/d)}{2\kappa_n^+}} - \psi}{\cos^2\alpha - \psi}}\right)\right]\right\}\cdot\cos\alpha. \qquad \text{(A68b)}$$

Therefore, we can draw contours with any ψ and κ_n^+ values, as a function of d in $x - y$ space.

For platy minerals, β is derived from Eq. (A65) as follows:

25

$$\beta = \cos^{-1}\left(\pm\sqrt{\frac{\sqrt{\dfrac{\ln d}{2\kappa_n^-}+\psi-1}}{\psi-\cos^2\alpha}}\right).\qquad\text{(A69)}$$

Thus, we have

$$x = \sqrt{2}\sin\left\{\frac{\pi}{4}-\frac{1}{2}\left[\cos^{-1}\left(\pm\sqrt{\frac{\sqrt{\dfrac{\ln d}{2\kappa_n^-}+\psi-1}}{\psi-\cos^2\alpha}}\right)\right]\right\}\cdot\sin\alpha\qquad\text{(A70a)}$$

$$y = \sqrt{2}\sin\left\{\frac{\pi}{4}-\frac{1}{2}\left[\cos^{-1}\left(\pm\sqrt{\frac{\sqrt{\dfrac{\ln d}{2\kappa_n^-}+\psi-1}}{\psi-\cos^2\alpha}}\right)\right]\right\}\cdot\cos\alpha.\qquad\text{(A70b)}$$

These parametric expressions are used to draw contours at any d value.

It is noted that upper- and lower-hemisphere projections for both columnar and platy minerals result in identical patterns of d at any $\kappa_n^{\pm}$ and ψ thanks to the symmetric rule.

References

Batschelet, E., 1981. Circular Statistics in Biology. Academic Press, London.

Fisher, N.I., 1993. Statistical Analysis of Circular Data. Cambridge University Press, Cambridge.

Hobbs, B.E., Means, W.D., Williams, P.F., 1976. An Outline of Structural Geology. John Wiley & Sons, New York.

Mardia, K.V., 1972. Statistics of Directional Data. Academic Press, London.

Terasawa, K., 1960. Sugaku-gairon. Iwanami, Tokyo. (Textbook on Mathematics written in Japanese)

Vernon, R.H., 2004. A Practical Guide to Rock Microstructure. Cambridge University Press, Cambridge.

von Mises, R., 1918. Über die "Ganzzahligkeit" der Atomgewichte und Verwandte Fragen. Physikal Zeitschrift 19, 490–500.